Design and Development of a Test Rig for Continuous Glucose Monitors (CGM)

Group 15

Department of Bioengineering

Imperial College London

A Project Report Submitted in
Partial Fulfilment of the

MEng Bioengineering Degree

Supervisors:
Dr.Anil Bharath, Dr.Anna Bird

Department of Bioengineering
a.bharath@imperial.ac.uk a.bird@imperial.ac.uk

Word Count: 4,945

April, 2025

Contents

Design and Development of a Test Rig for Continuous Glucose Monitors (CGM)

Russell Guo, Evan Hammerstein, Boyang Li,

Linda Schermeier, Noah Weiler, Tianrui Yue

April 15, 2025

Abstract

Continuous glucose monitors (CGMs) are rapidly becoming the standard of care in diabetes management. However, despite their growing clinical relevance, CGMs still face significant limitations—such as signal interference from medications and sensor degradation over time—that can compromise accuracy and reliability. These challenges underscore the need for effective, rapid, and low-cost evaluation methods during the early stages of CGM development. However, published in-vitro tests typically rely on repeated trials with large human and time input on creating specific test conditions. In response, this study aims to design a cost-effective, automated and programmable test rig which can realize physiologically meaningful test conditions for commercial CGMs. Two test rigs were eventually designed and implemented after parts optimization. Both systems integrate Arduino-based controllers with custom syringe and peristaltic pumps, passive mixers, and CGM-compatible sensor interfaces. Control algorithms were designed to emulate glucose dynamics under varied physiological conditions by incorporating existing mathematical model. Comprehensive validation was conducted. Pump flow rates were shown to be consistent across RPM settings, and mixer performance was confirmed via spectrophotometer absorbance spectrum analysis. The CGM interface demonstrated leak-free operation and stable sensor signal acquisition over time. Software logic is verified by testing on glucose profile generated by the Padova model, although integration trials revealed incompatibilities between software control protocols and certain hardware components, suggesting areas for further refinement. These platforms provide a flexible and time-saving environment for early-stage CGM prototyping, supporting faster innovation cycles and broader access to affordable, high-performance glucose monitoring technologies.

1 Introduction

1.1 Project Overview

Over the past decade, continuous glucose monitors (CGMs) have seen growing interest among healthcare providers and patients. Used for standalone glucose monitoring or within closed-loop insulin delivery systems,

CGMs have become the new standard of care, especially in outpatient settings [1]. Despite recent advances, several challenges remain – such as interference of concomitant medication and sensor degradation over time – which can compromise accuracy [2][3]. This highlights the need for improved sensor designs capable of mitigating such issues and effective and efficient testing methods for rapid prototype development. Published in-vitro testing typically relies on repeated trials using manually prepared glucose solutions at limited concentration ranges, requiring human effort and time [4][5]. An efficient test rig capable of making automated adjustments to the testing environment, thereby reducing human effort in CGM prototype evaluations, could accelerate early-stage development. Comprehensive in vitro testing should be leveraged to detect problems early, reducing the number of clinical studies conducted on flawed prototypes. Previous studies have explored automated CGM test rigs, including one study which suggested a test rig design based on high-pressure liquid chromatography (HPLC) pumps [6]. In this setup, CGM sensors were housed in fluidic channels connected to HPLC pumps, maintaining constant contact with the fluid. The channel could accommodate up to six sensors for simultaneous testing of multiple devices. To study interference from concomitant medications, three separate HPLC pumps supplied the fluid channel with buffer solution, glucose stock, and different candidate substances. By varying the flow rates of different solutions into the testing channel, programmable glucose gradients were achieved. This configuration successfully identified interference from several commonly used drugs. However, despite the system's success, the high cost of HPLC pumps limits its use in small-scale tests. Additionally, this design still requires significant human input and specific knowledge for HPLC pump programming. Moreover, although this design enables sequential testing of CGMs at various glucose concentrations, it fails to replicate physiological glucose level variations. In the human body, blood glucose depends on physiological events like food ingestion, exercise, and basal metabolism, which the existing test rig cannot mimic. Since CGMs are ultimately intended for use within the human body, neglecting physiological processes during testing may lead to inaccurate or unrepresentative results.

1.2 Main Objectives

Having identified the limitations of the existing CGM test rig design, four major aims are targeted in this study:

- To design a test rig using cost-effective, standardized, readily available, and easy-to-assemble components, to make the test rig financially feasible and deployable for small-scale pilot studies.
- To incorporate established mathematical models [7] to mimic the dynamic progression of blood glucose within the human body, accounting for biological processes involved in glucose regulation.
- To automate a fluid control system that delivers varied glucose concentrations to the sensor while minimizing the need for manual adjustments.
- To develop a user-friendly interface that translates user inputs into test rig operations, while also automatically collecting and visualizing data from CGM during testing.

2 Background

2.1 Fluid Delivery System

A key subsystem of the test rig is a fluid delivery system, as the source of flow for the test rig. Ideally, the system should automatically adjust glucose concentrations based on user inputs, fulfilling the third design aim. Such fine-tuned control requires the system to interface with programmable digital controllers capable of providing precise commands. The system also ideally should be able to generate dynamic glucose concentrations instead of limited fixed values to precisely and smoothly realise the physiological glucose level variations. Due to the low flow rate (around $10^{-1}\mu L/min$) of interstitial fluid (ISF), the primary medium for CGMs [8][9], a flow rate range that is compatible with the CGM must be implemented to prevent damage and ensure accurate readings. 1mL/min was determined by the mentioned HPLC pump design as a suitable experimental flow rate [6].

As a common option for fluid delivery, peristaltic pumps have been used in a similar prototypical test rig design for CGM testing, but with limited usage details [10]. One open-source peristaltic pump design can be

assembled from 3D-printed components and commercially available parts, making it both cost-effective and highly customizable [11]. While being programmable via a microcontroller, this design can provide a maximum flow rate up to 1.62 mL/min with 3mm tubing.

Syringe pumps have been used to simulate ISF flow to study angiogenesis [12], making it potentially compatible with CGMs designed to work in the ISF. Common syringe pumps support a flow rate range well-fitting the 1mL/min value identified by the mentioned research and can be programmable via serial communication with a computer [13].

2.2 Fluid Flow and Mixing

The fluidic system must meet certain design requirements to ensure reliable operation and accurate CGM readings: leak-free operation; effective fluid mixing; and cost-efficient, manufacturable components. Standardized Luer lock and slip connectors can be used with silicone rubber tubing to ensure uniform flow characteristics and leak-free, interchangeable connections throughout the system [14]. The Reynolds number Re quantifies the ratio of inertial to viscous forces and helps classify three types of flow regimes (See Figure 1a). This system operates under low Re conditions due to its flow rate of 1 mL/min [4], with a maximum Re of approximately 13.6 (See Appendix D). At these low values, the flow is laminar, meaning predictable but poorly mixed flow.

One approach to improve mixing under these conditions is to introduce curvature into the tubing's geometry, thus increasing the Dean number De. The Dean number accounts for secondary flow development in curved geometries, specifically the creation of Dean vortices (See Appendix F). These vortices arise due to centrifugal effects in curved channels and promote transverse mixing. The effect of curved geometries on streamlines is shown in Figure 1b. Higher Dean numbers correspond to stronger secondary flows and, therefore, to more efficient mixing.

An alternative approach to mixing was also investigated. Rather than relying on the creation of Dean Vortices, successive rotation and reversal of the flow disrupts the laminar streamlines and promotes mixing through flow reorientation rather than Dean vortex formation [15].

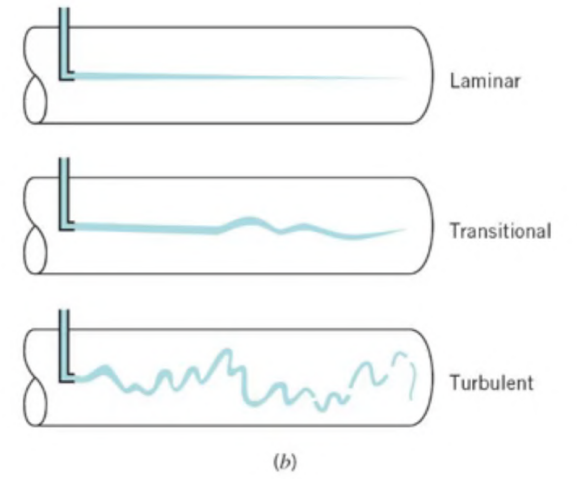

(a) Different flow regions based on Re number.[16]

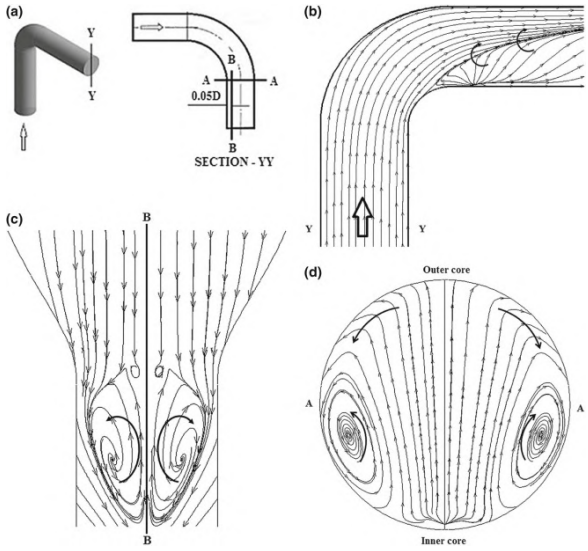

(b) Magnified view of streamlines as fluid goes through a bend, creation of secondary flows (Dean vortices). [17]

Figure 1: Illustration of different flow types based on different dimensionless parameters.

2.3 CGM Interface

There is a precedent to integrate commercially available CGMs into fluidic test rig systems. Salazar et al applied CGM for continuous inline monitoring of glucose in an organ-on-chip. The system featured a 3D-printed culture chamber that housed encapsulated live cells. The CGM is fixed on top of the 3D-printed chamber and is used to measure the changing glucose concentration to reflect the organ-on-chip metabolic performance [18]. While this is an example of a functional application of CGMs in an integrated system, in the mentioned HPLC-based test rig, where the whole system is built for CGM validation, CGMs were directly fixed to an open fluidic channel. The gap between the CGM and T-connector is filled by chemically inert cotton [18]. In both cases, the CGM interfaces adopt a design with a leak-proof and secure connection to the CGM and minimize fluid buildup by introducing consistent flow. A leak-proof connection is vital to maintaining the expected pressure and flow rate in the system, and a secure connection prevents the CGM from being damaged by the fluid. Minimizing fluid buildup ensures efficient substance exchange around the CGM filament, which means system concentration changes can be reliably sensed by CGM.

2.4 CGM Sensing

CGMs measure glucose concentrations in the interstitial fluid (ISF) via a small sensor inserted under the skin. Most commercial CGMs, such as Freestyle Libre, utilize immobilized glucose oxidase (GOx), which reacts with glucose [19] to create an electrical signal that is proportional to the glucose concentration [20]. In aqueous solutions, such as ISF, glucose exists as beta (ca. 63%) and alpha (ca. 37%) anomers [21]. GOx exhibits specificity for the beta anomer of glucose, which can lead to underestimation of true glucose levels [22]. This guides the design of the testing method in Section 3.4.

3 Methods

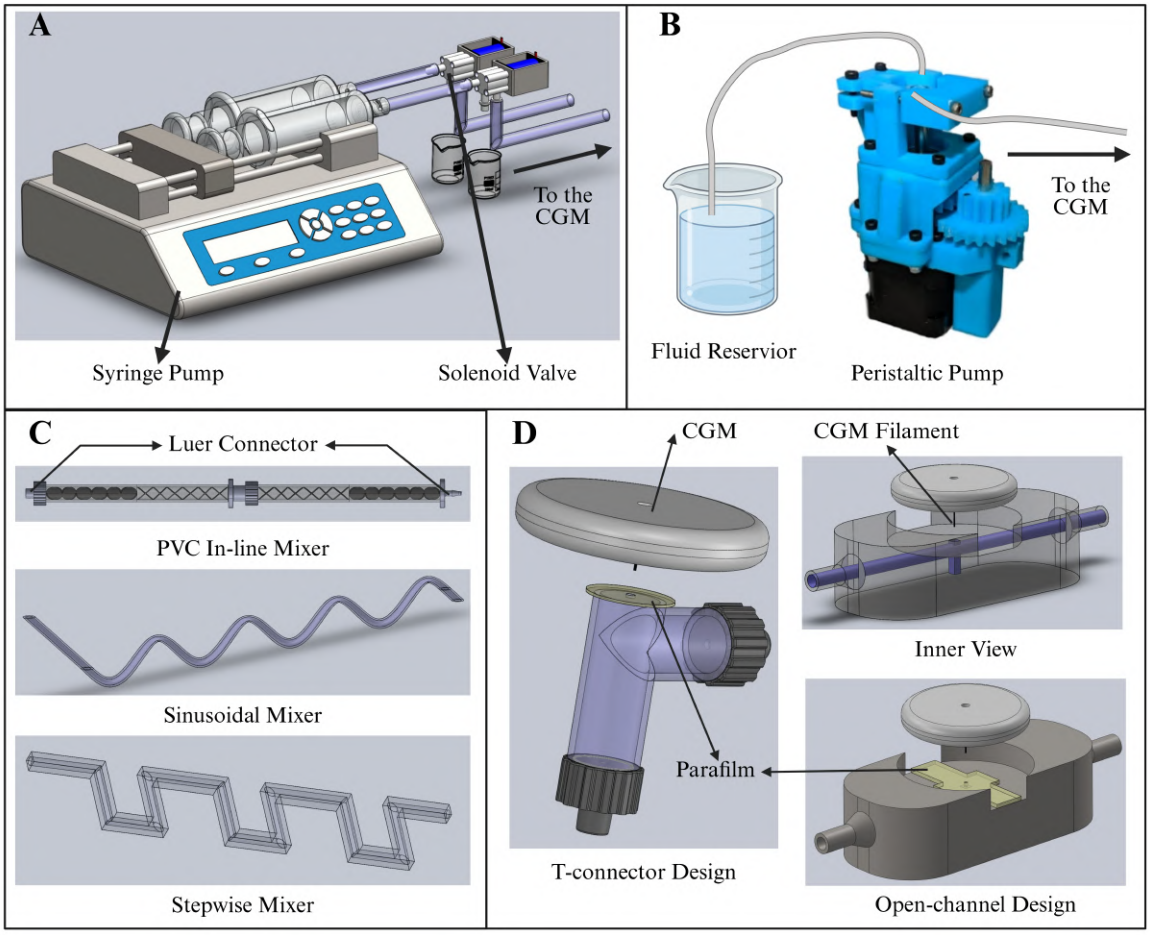

Figure 2: Designs of customized components. (A) 3D assembly of the overall binary system design. (B) Open-source peristaltic pump design. (C) 3D models of passive mixer iterations. (D) 3D model of sensor interface and CGM housing.

3.1 Mixer Protocol

3.1.1 Mixer Design and Manufacturing

All mixers designed (Figure 2C) are passive mixers, which achieve mixing through geometrical features rather than external energy input. Their geometries are optimised to enhance mixing at low Reynolds numbers.

Two passive mixer designs were developed to enhance mixing based on the creation of Dean vortices: a stepwise mixer, where a circular tube is enclosed in a square casing following a step profile, and a sinusoidal mixer, where a hollow pipe follows a sinusoidal path, both 3D-printable. These designs use repeated bends to stretch, fold, and rotate the flow, increasing interfacial contact through chaotic advection [23].

The third passive mixer, a 3D-printable helical in-line mixer, was developed to introduce flow reorientation and disruption of laminar streamlines via helically arranged blades with alternating 90° orientations [15]. To ensure full disruption of the streamlines, the mixer was designed as a repeatable module using male and female Luer connectors (top of Figure 2C).

All mixers were designed in SolidWorks and 3D-printed using a Prusa i3 MK3S+ printer with polylactic acid

(PLA) filament at 0.1mm layer-height (apply for all 3D printing in this study). The mixing element for the helical in-line mixer was adapted from GrabCAD. See Appendix I for the CAD files of this system [24].

3.1.2 Absorbance Testing

A diluted red dye solution was prepared by mixing 0.5 mL of red dye (detailed in Appendix J) with 150 mL of deionized water. This concentration was selected to fall within the measurable range of the Jenway 6305 spectrophotometer [25]. Two 30 mL syringes, one filled with the diluted red solution and the other with water, were mounted on a Harvard Apparatus PHD 2000 syringe pump. Both syringes were set to infuse at a flow rate of 1.1 mL/min. The output from the syringes was passed through one of the mixer designs and collected in a cuvette, which was immediately inserted into the spectrophotometer for absorbance measurement (400-900nm). The procedure was repeated under identical conditions but without the mixer to serve as a negative control.

As a positive control, 10 mL of diluted red solution and 10 mL of pure water were combined, ensuring the same 1 to 1 ratio as the syringe pump system employs, and magnetically stirred for 10 minutes to ensure complete mixing before measurement.

Due to the colour of the red dye, the region between 700 to 875nm was chosen as the region of interest (ROI) [26]. This range should encompass the expected measured absorbance peak, which is critical in assessing mixer efficiency, as measurements at the peak wavelength provide the highest sensitivity and should thus reveal any discrepancies between spectra.

3.2 CGM Interface Manufacturing and Testing

Based on the research outlined in Section 2.3, two interface designs were developed and displayed in Figure 2D. The right of Figure 2D displays an open-channel design adapted from the discussed chip design [4]. Multiple bottom chamber sizes were tested to potentially minimize the buildup volume. The groove is included at the top surface to secure the CGM, and self-sealant Parafilm® (Merck) is applied to the hole to prevent leakage while allowing penetration for CGM insertion [27].

The other tested design option, based on commercially available T-connectors (see Appendix F for T-connectors used), is shown on the left of Figure 2D, which allows fluid inflow and outflow through side and bottom Luer locks. Parafilm covers the top as a CGM insertion site and a leakage-proof sealant. No external housing is provided for CGM fixation; hence, the connection security will be investigated.

Both designs are developed using SolidWorks and 3D-printed using the mentioned printing protocol. Since the key aim of the CGM interface is to support CGM readings and integration into the overall test rig system, both interfaces are tested following the same protocol as the integrated system testing outlined in Section 3.4.2. The evaluation of design performance will depend on the CGM insertion status. The leakage condition was also recorded.

3.3 Peristaltic Pump Protocol

3.3.1 Pump Assembly

For assembling the open-source pump, the parts list was consulted in the GitHub repository [28]. The parts consisted of commercially available mechanical parts and 3D-printed parts, printed using a Prusa i3 MK3S+. The assembly instructions and complete parts list can be found on the GitHub repository [28], or in Appendix G. Some light machining, including a lathe and filing, was necessary for alterations of the metal shafts used in the design. Many part alterations were made according to the system's specific design and scale; the modelling edits were contributed to the repository (see Appendix E). These changes are further detailed in 5.2.

3.3.2 RPM to Flow Rate Mapping

The peristaltic pump must be calibrated after assembly by experimentally determining the relationship between stepper motor rotation speed and volumetric flow rate. To test this, a pump was first run with 10 mmol/L glucose solution at 20 RPM for one hour to ensure functionality. Tests were conducted at 10 discrete motor speeds ranging from 15 - 150 RPM. For each speed, the pump operated for 10 minutes, and the mass of the outflow was measured by an analytical balance. Volumetric flow rate (mL/min) was calculated by dividing each final weight by the density of the glucose solution (1.0218 g/mL) and averaging over the trial duration. A sample data processing calculation is provided in Appendix E.

The theoretical volume displaced per unit time (the flow rate Q) is expressed by (1).

$$Q = V_{\text{displaced per revolution}} \times \text{RPM} \tag{1}$$

Where the volume displaced per revolution is proportional to the cross-sectional area of tubing, with radius, R, and the length of tubing compressed during each revolution, L, as described in (2).

$$V_{\text{displaced per revolution}} = \pi \times R^2 \times L_{\text{compressed tubing}} \tag{2}$$

The length of compressed tubing is calculated from the amount of tubing in contact with ball bearings (3 in this case), each of which interfaces with the tubing for an estimated third of its circumference. Therefore, the expected value in this case is calculated in (3).

$$V_{displaced\ per\ revolution} = \pi \times (0.00075)^2 \times 3\left(\frac{\pi \times (0.009525)}{3}\right) \times 10^6 = 0.0528 \text{ mL/rev} \tag{3}$$

3.4 Software Integration

For the binary profile, an Arduino-based C++ program was implemented to alternate between two valve control configurations, flexible for other applications. Each valve controls a different fluid of a certain glucose concentration, directing flow into the rest of the system while the other is diverted into a waste beaker.

For the dynamic profile, a control algorithm for an Arduino was written for a two-peristaltic pump system, establishing a new open-source repository, found in Appendix E, along with other novel designs. These algorithms were tested with the user interface (made using Electron) to collect user-input parameters, and simulate the following values:

- Composite Flow Rate at Sensor Interface = 10 mL/min
- Inner Diameter of Tubing = 1.5 mm
- Length of Tubing before mixing intersection = 10 mm
- The glucose concentrations of the two fluid reservoirs = 15.0, 0.0 mmol/L
- Simulated Glucose Profile = Adult #0006

From these parameters, the algorithms calculate the necessary flow rate, RPM, and delay of the pumps for each time point in the profile. A logical flowchart is presented in Figure 3.

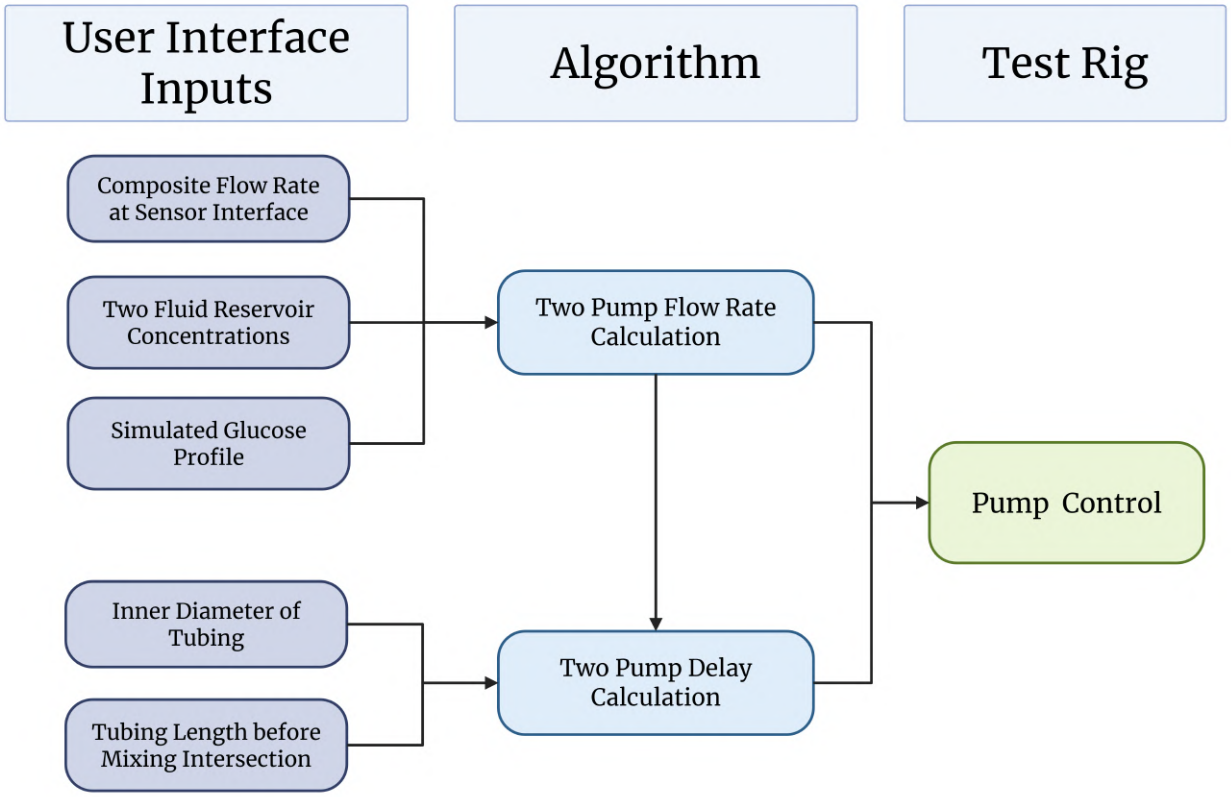

Figure 3: Conceptual illustration of the pump control algorithm. Three inputs (dark blue) are used to calculate the pump flow rates, whilst two others are used to calculate the required delay, both of which control the pumps.

The simulated glucose profile is created by an open-source Python implementation (found in Appendix E) of the Padova model[29], a realistic simulator for glucose profiles. Researchers can input mealtimes and amounts, and the system generates a 24-hour glucose concentration profile over time. The first two hours of an example patient database profile generated (adult#0006.csv) were simulated.

3.5 Integrated Systems

3.5.1 System Integration

Two systems are eventually integrated: binary and dynamic, which are illustrated in Figure 4. For the binary system, a two-syringe syringe pump is used to deliver fluid, which is connected to two solenoid valves (SourcingMap) controlled by the microcontroller (Kona328, Orangepip). Flow passes through the CGM interface, triggering glucose readings which are recorded and viewed via the CGM reader (xDrip+ with Android phone).

For the dynamic system, two peristaltic pumps are used, also controlled by a microcontroller (Uno, Arduino). The fluids join at the passive mixer, which homogenizes them, and finally reach the CGM interface, where CGM readings are recorded using the same CGM reader.

All the intersecting connections for both systems are enabled by Y-connectors (Vygon). Luer connectors are used for connecting different fluidic components throughout the system. See Appendix F, G, and O for details of materials used and circuit diagrams for both systems.

To generate a dynamic glucose concentration profile through software control, two pumps were employed to deliver high- and low-concentration glucose solutions at independently regulated flow rates. These streams converge at a Y-junction, where they mix to form an intermediate concentration.

Delayed initiation calculated in the algorithm was implemented to ensure synchronized arrival of both streams at the junction, facilitating stable and homogeneous mixing. By continuously adjusting the flow rate ratio between the two pumps, the system is capable of modulating the output concentration in real time. This enables the control algorithm to follow a predefined target concentration trajectory, thereby allowing programmable and dynamic solute delivery throughout experimental protocols.[30]

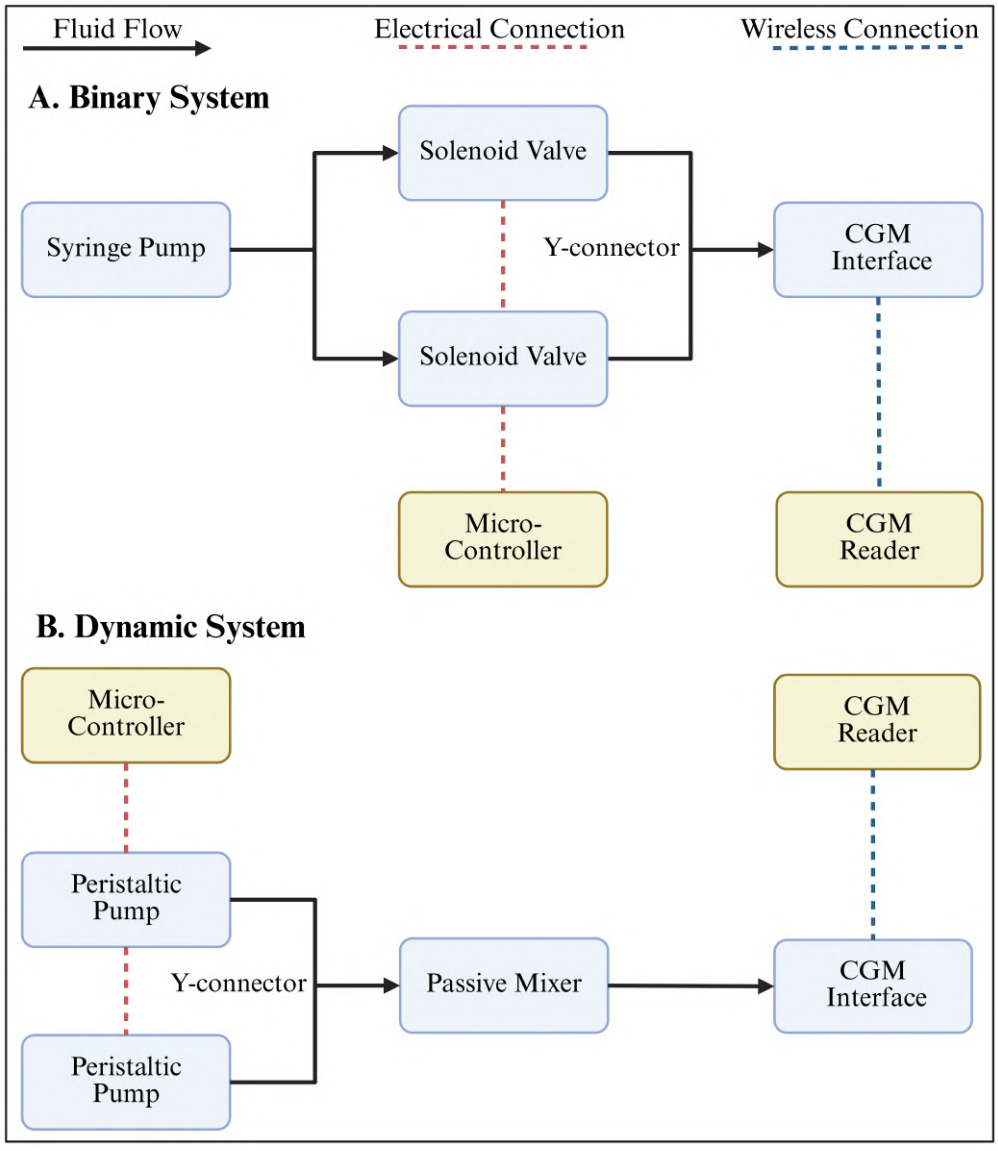

Figure 4: Conceptual illustrations on integration of binary (A) and dynamic (B) systems. Note that blue and yellow blocks represent fluidic and electronic components, respectively.

3.5.2 Integrated System Testing

To further characterise the system behaviours, both systems were tested using a commercially available CGM model (FreeStyle Libre 2+, Abbott). Preliminary CGM readings from xDrip+ in different glucose solutions suggest using a 10-20mmol/L test range to stay within the sensor's target range (3.9-10.0mmol/L) [31]. Additionally, control tests were conducted by placing the CGM directly into glucose solutions of constant concentrations (15 and 20 mmol/L).

For the binary system, the syringe pump is loaded with two 50 mL syringes, containing 15 and 20 mmol/L glucose solutions. The solenoid valves are programmed such that each solution is alternately delivered to the CGM interface for 30 minutes at a time.

Regarding the dynamic system, two peristaltic pumps are connected to reservoirs containing 10 mmol/L and 20 mmol/L glucose solutions. The flow rate ratio between the pumps is dynamically adjusted through the control algorithm on the microcontroller to achieve the target glucose concentration. The custom glucose profile can be found in Appendix H.

Data was recorded for 2 hours for both systems, where the obtained glucose profile readings from xDrip+ are compared with the theoretical input profiles. The difference between actual readings and the target profile indicates the performance of the overall fluidic systems. Note that all glucose solutions use phosphate-buffered saline (Merck) as solvent.

4 Results

4.1 Mixer Manufacture and Testing

The manufacturing and testing results of Section 3.1 are displayed in Figure 5. Note that A-C have unremovable internal supports that are not visible. The three absorbance spectra are displayed in E, with the only small disparity occurring at 720nm for the Y-junction test.

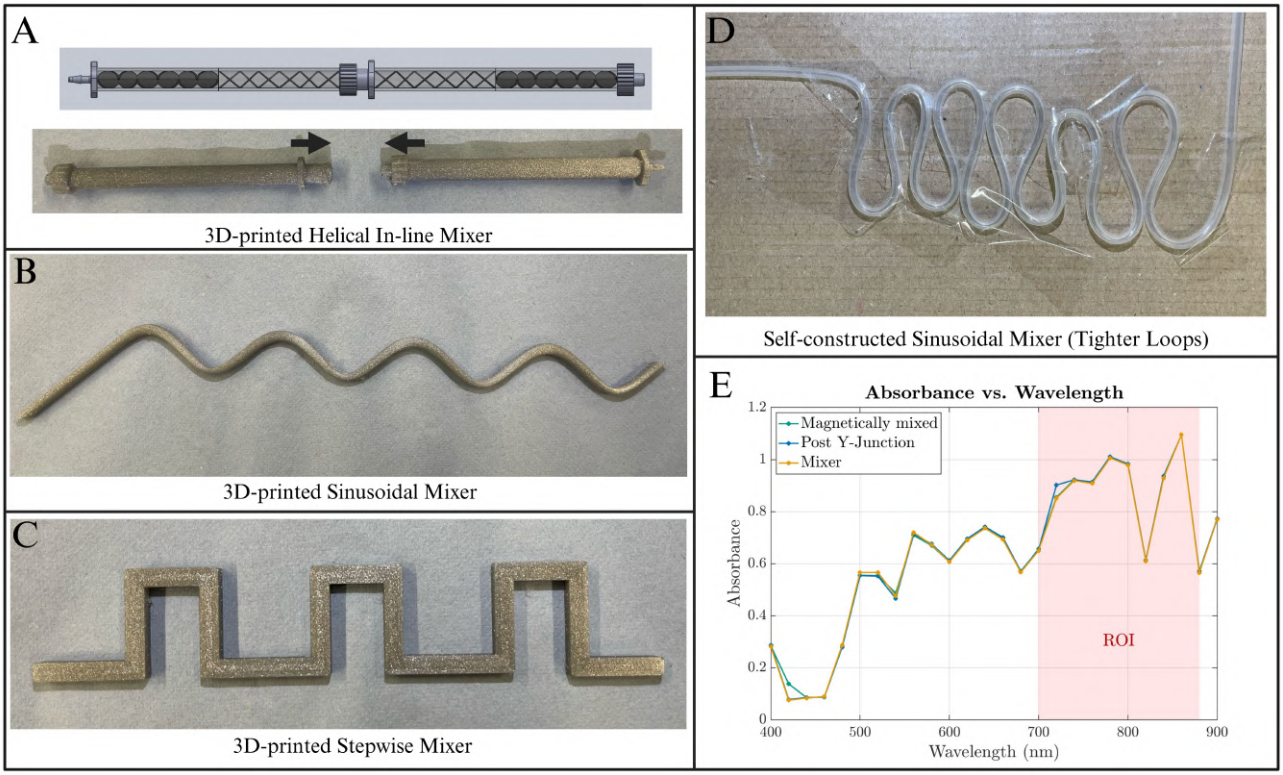

Figure 5: (A) CAD model of the helical in-line mixer and the 3D-printed results. Black arrows denote the Luer connection of the mixer ends. (B) Photo of the 3D-printed sinusoidal passive mixer. (C) Photo of the 3D-printed stepwise mixer, (D) Photo of the self-constructed sinusoidal passive mixer, (E) Graph of absorbance measurements using different mixing methods with highlighted ROI. "Magnetically mixed" represents the well-mixed positive control condition. "Post Y-Junction" denotes the flow condition without a mixing structure. "Mixer" corresponds to the self-constructed mixer described in panel (D).

4.2 CGM Interface and Stock Solution Testing

Results for the CGM interface manufacturing and stock solution test of Section 3.2 and 3.5 are shown in Figure 6. Parafilm collapse exists for the T-connector design (Figure 6B), which also had noticeable leakage during testing (not shown in the figure). These conditions weren't observed for open-channel design (Figure 6A). For CGM stock solution testing, increasing trends were observed for both tested concentrations (Figure 6C).

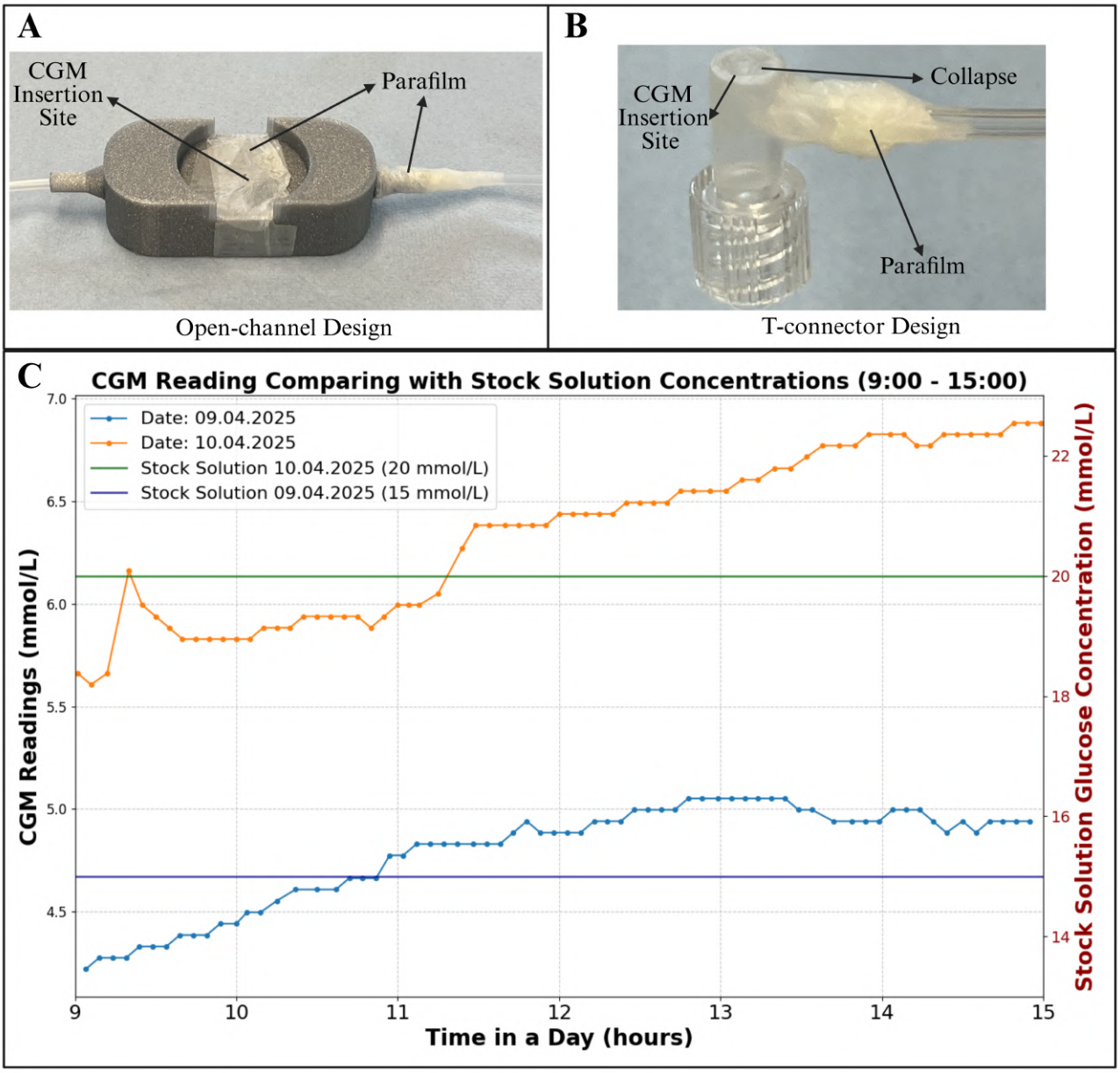

Figure 6: (A) An open-channel design for CGM attachment is illustrated. Parafilm is wrapped around the air interfaces to achieve a sealing effect. The left nozzle end is shown exposed to demonstrate the tubing connection, while the right end displays the appearance after wrapping. A hole is visible at the center, where the CGM filament is inserted and immersed in the fluid. (B) An alternative design using a T-connector is shown. Noticeable Parafilm collapse after sensor application is labeled. (C) Sensor readings recorded by xDrip+ while the CGM was immersed in glucose stock solutions: 15 mmol/L on 09/04/2024 and 20 mmol/L on 10/04/2024, both measured from 9:00 to 15:00.

4.3 Peristaltic Pump Manufacture and Mapping

The manufacturing and mapping results of the peristaltic pump are displayed in Figure 7. Panel A outlines the unexpected design changes that were necessary for a functional pump, outlined in detail in 5.2. In Panel B, the flow rate displays a strong positive linear correlation with RPM (Pearson's r = 0.9998).

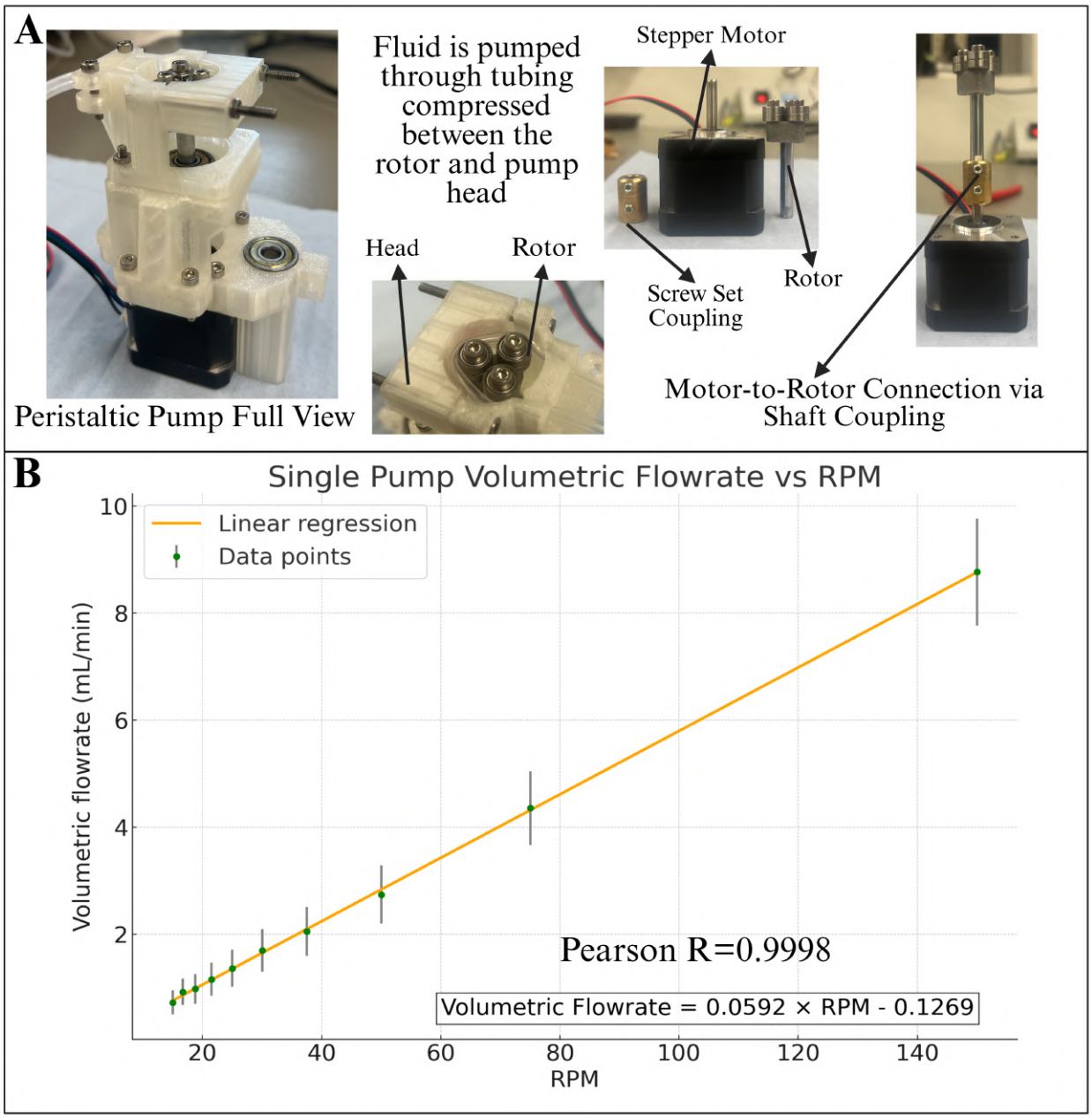

Figure 7: Completed peristaltic pumps and performance characterization. (A) From left to right: the first image shows the fully assembled pump; the second illustrates the tube compression pumping mechanism; the third and fourth depict our design modifications. The original design is provided in Appendix E. (B) Relationship between pump revolution rate (RPM) and volumetric flow rate for a single pump.

4.4 UI to Control Algorithm Testing

The user interface as well as an example simulated glucose profile, are displayed in Figures 8A and 8B, along with the theoretical algorithm outputs in 8C. Note that a similar shape is shared by the progression of RPM and flow rate. Pump C1 and C2 remain complements to each other throughout the time period. A similar shape is also shared between the pump delay progression and the segmented generated glucose profile.

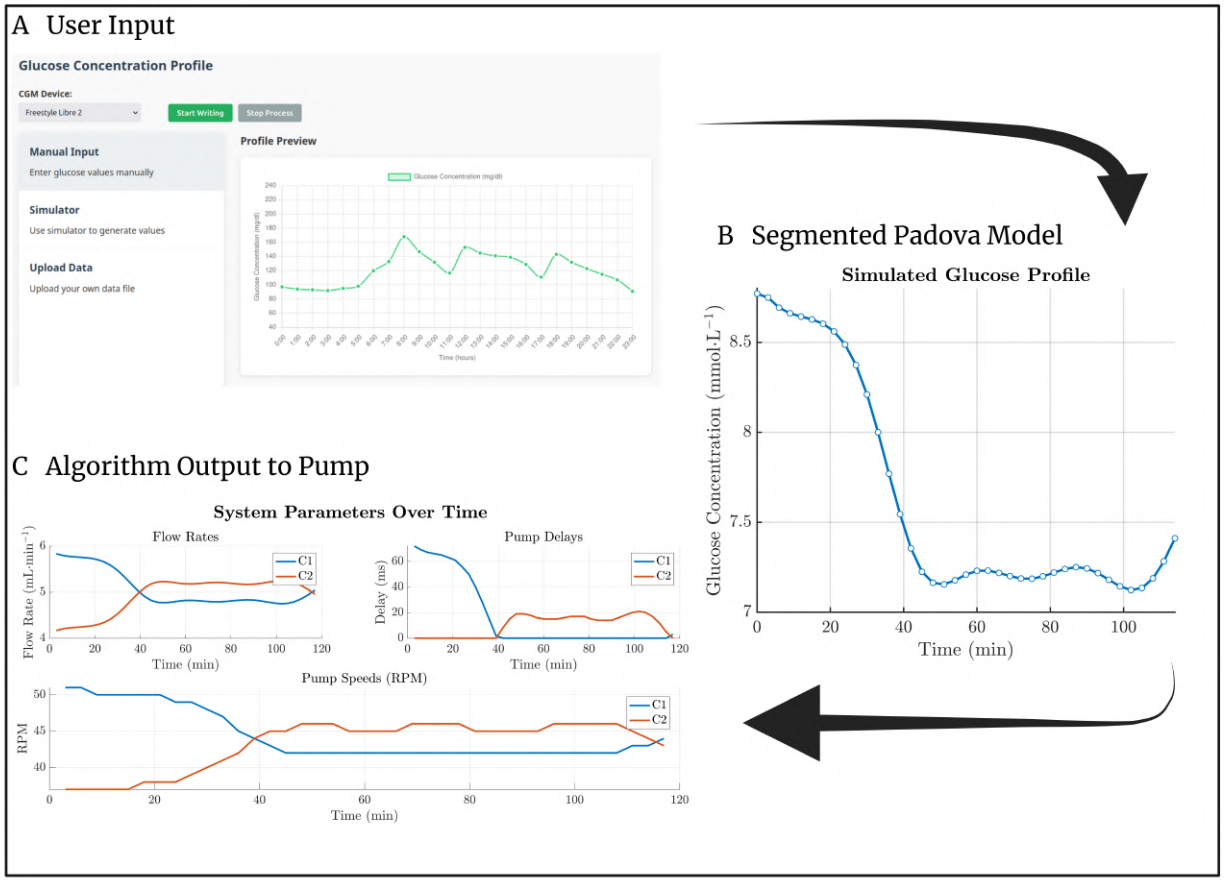

Figure 8: **System overview for generating pump control parameters from a target glucose profile.** (A) A user-defined or simulated glucose concentration profile is input through the UI. (B) The Padova Model is segmented to generate a target glucose trajectory over time, which is input into the algorithm. (C) The control algorithm computes the flow rates of solution C1, the higher concentration solution, and C2, the lower concentration solution, associated pump delays, and RPM values required to recreate the target profile using the specified dynamic system.

4.5 Binary and Dynamic Test Rig Setup and Results

The setups with labeled components for both tested systems are shown in Figure 9A and 9D. Parts lists can be found in Appendices F and G. The comparison between the input and output profiles is shown in panels 9B and 9C. There is a clear correlation between the trends of input and output.

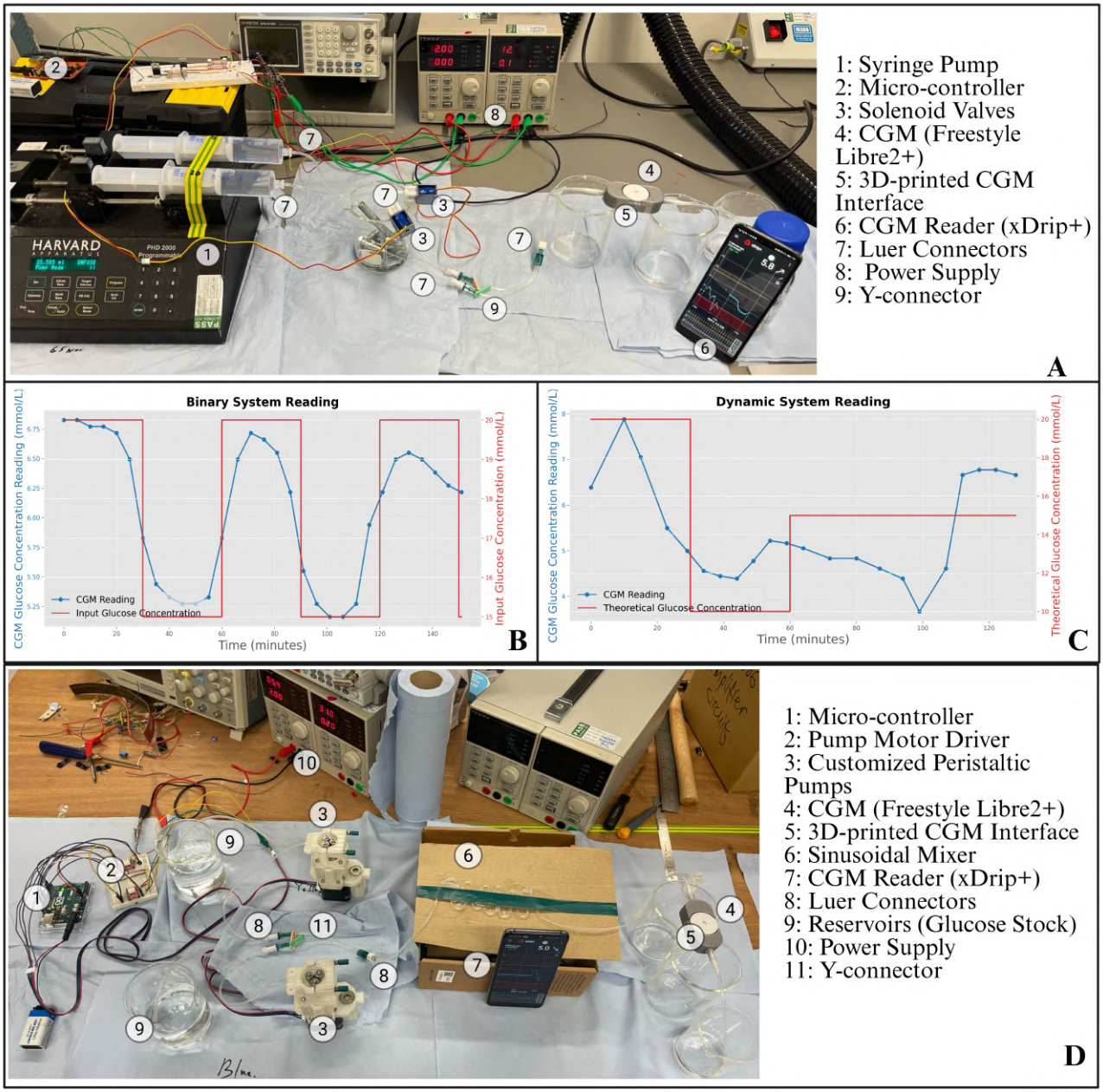

Figure 9: (A) shows the labelled binary system setup. (B) shows the glucose concentration measured by the Freestyle Libre 2 CGM (blue) compared to the input profile (red) for the binary system. (C) shows the glucose concentration measured by the Freestyle Libre 2 CGM (blue) compared to the input profile (red) for the dynamic system. (D) shows the labelled dynamic system setup.

5 Discussion

As the demand and need for CGMs increase, researchers must be equipped with increasingly efficient systems to accelerate development. This research aimed to create a test rig that aids with CGM accuracy testing in a controllable, robust, and easily accessible manner.

5.1 Mixing Effectiveness

As shown in Figure 5(A-C), the 3D-printed mixer designs required internal supports that were difficult to remove without damaging the structure. Others were too small to print with the 0.1mm resolution of the standard-resolution printers commonly in research labs. Higher-resolution printers required for these mixers may be inaccessible in typical research facilities, making 5A-C suboptimal for the system. As a result, the self-constructed mixer shown in Figure 5D was designed to allow for easy assembly using the same silicone tubing used throughout the system. Its performance was evaluated, as shown in Figure 5E. The absorbance of the mixer was identical to the magnetically stirred sample across all wavelengths, especially within the region of interest, proving that Mixer D is an accessible and effective choice. The absorbance of the upstream Y-junction was also measured. Measured values exhibited a smaller difference than anticipated, with only a small discrepancy in measurements around the region of interest (720 nm). More trials in the future are essential for complete confidence, as the discrepancy could have been caused by error or environmental conditions. However, the wavelength at which this occurs suggests that any mixing capability difference would display at that wavelength, concluding that the Y-junction contributes to mixing but is insufficient on its own. Therefore, due to its simple implementation and effectiveness, Mixer D remains a preferred component in the system to ensure a fully homogenous fluid reaching the CGM interface. The performance of each mixer is summarised below in Table 1.

Mixer Design	Easily Fabricated	Resulting Effective Mixing	Leak Proof	Advection-Based
Stepwise Mixer (Square-wave bends)			✓	✓
Sinusoidal Mixer (Wavy channel)			✓	✓
Self-Constructed Mixer (Multi-loop)	✓	✓	✓	✓
Helical in-line mixer			✓	

Table 1: Comparison of four inline mixers against performance criteria.

For future work, it is important to consider that diffusion may also contribute to mixing, given the small scale (1.5mm ID) of the system, resulting in laminar flow (low Reynolds' Number) that, without the introduction of chaotic advection, relies on concentration gradients to mix. The effects of diffusion can be investigated by replacing Mixer D with a straight tube of equal length for comparison. Similarly, as diffusion is time-dependent, increasing the flow rate helps distinguish the mixing mechanisms, as a greater absorbance spectrum divergence would suggest the mixing was more diffusion-driven rather than mixer effectiveness.

5.2 Open-Source Peristaltic Pump Performance

As shown in Figure7A, the pump was successfully assembled with minor modifications to reduce mechanical vibrations and structural instability observed during operation (see AppendiX N for details of the modifications). The mapping protocol, illustrated in Figure 7B, demonstrated a strong linear relationship between stepper motor RPM and flow rate, with a correlation coefficient of $R = 0.9998$. As discussed in Section 3.3.2, the theoretical volumetric displacement per rotation, represented by the slope of the curve, closely matched the experimental data. The theoretical value was approximately 89% of the experimental result, likely due to an underestimation of the arc contact length between the rotor and the tubing. Despite this discrepancy, the mapping results are sufficiently accurate for implementation within the control algorithm.

For future improvements, increased flow rate variance was observed at higher motor speeds, attributed to loosening of the pump head's securing nuts. Elevated RPMs intensified vibrations, gradually loosening the nuts and altering contact pressure between the pump head and rotor. This affected the compression of the tubing, causing irregular deformation and inconsistent flow rates. Although the CGM test rig operates at lower RPMs

(1–2 mL/min) where this effect is minimal.

5.3 CGM Interface

For the T-connector design (Figure 6B), Parafilm collapse, possibly due to a small contact area with the interface, may cause sealant failure, which explains the leakage recorded during the testing. A secure connection is also not supported due to no external fixation housing for the interface. Additionally, the fluid buildup can't be minimized due to the fixed chamber volume of the T-connector.

Regarding the open-channel design (Figure 6A), the integrity of the insertion site is maintained after 2-hour integrated testing, supporting non-leakage observation. A secure connection can be justified by fitting a groove for CGM. Theoretically, the fluid buildup can be minimized by reducing the bottom chamber volume, illustrated in the inner view of Figure 2D.

Both interfaces adopt a 3D-printable design or commercially available parts, ensuring accessibility under common lab conditions. The designs and their adherence to the design criteria are summarized in Table 2. Therefore, the open-channel design is proven to surpass the T-connector design and was integrated into both binary and dynamic systems, which were tested.

Interface Design	Minimized Fluid Buildup	Leak-Proof	Secure Connection with CGM	Accessibility
Open-channel Design [18]	✓	✓	✓	✓
T-connector Design [32]				✓

Table 2: The interface options with their expected adherence to design criteria

5.4 Software Algorithm Analysis

On the software side, the UI shown in Figure 8A creates a simple way for researchers to tailor the system to their needs. Figure 8B shows an example Padova profile that would be simulated in the algorithm, with Figure 8C showing the corresponding calculated pump control parameters. The algorithm is performing in line with its expected behaviour, including:

- The sum of the flow rates remains constant.
- A non-zero delay is only output for the faster pump, as shown at Time = 40 mins, where the C2 pump eclipses C1.
- The RPM/flow rate graphs exhibit identical shapes, proving that mapping was implemented successfully.
- To demonstrate correct flow rate calculations, sample calculations for the first time point are shown in Appendix L

The program was tested with edge cases as well, when the simulated concentration is equal to one of the starting concentrations, creating zero flow from one pump. While this initially caused a DivisionByZero error during delay calculation, appropriate error handling was implemented to handle such cases.

However, during system integration, certain experimental parameters resulted in a correct, but unusable system using this algorithm. As shown in Figure 8C, the system delay increases sharply when the target concentration approaches one of the initial concentrations. In such cases, the algorithm assigns an extremely low flow rate to one of the pumps, resulting in delays on the order of minutes to hours rather than milliseconds. An illustrative calculation of this behavior is provided in Appendix P. Although this issue can render the system impractical under certain parameter combinations, it can largely be mitigated through careful initialization of

the starting concentrations.

Future work in this area includes creating an algorithm that calculates the two ideal starting concentrations for the profile to minimize delay and output the maximum delay in this case.

5.5 Comparison of Discrete and Dynamic Systems

For the binary system (Figure 9B), the theoretical glucose input followed a square-wave pattern alternating between 15 mmol/L and 20 mmol/L at 30-minute intervals. The CGM successfully tracked the intended trend, with recorded values oscillating between approximately 5.1 mmol/L and 6.8 mmol/L. Although the CGM output followed the square-wave profile, two key discrepancies were noted.

First, the absolute CGM readings did not match the input concentrations. As discussed in Section 2.4, this deviation aligns with the CGM's known sensitivity to β-glucose, which constitutes approximately 63% of the total glucose concentration. This supports the interpretation that the CGM internally estimates blood glucose values to reflect physiological conditions, though environmental variables such as temperature—uncontrolled in this in-vitro setup—may also contribute.

Second, the CGM response displayed smoothed transitions at the rising and falling edges of the theoretical square wave. This smoothing may be attributable to diffusion delays within the sensor membrane. Additionally, the uniformity of the transitions suggests the possibility of internal signal processing, such as averaging or interpolation algorithms, though this remains speculative in the absence of direct evidence.

For the dynamic system (Figure 9C), the control algorithm was designed to adjust the flow rate ratio of the two input pumps in real time to achieve a target glucose concentration. The CGM readings generally followed the intended trend, demonstrating the effectiveness of algorithm-driven mixing. However, due to the parameter settings used—resulting in substantial output delays as discussed in Section 5.4—the original target profile had to be replaced with a simplified, less physiologically realistic version (Appendix H).

Despite this adjustment, the mismatch between the theoretical glucose profile and the CGM readings was more pronounced than in the binary system (Figure 9B). This discrepancy may be attributable to the increased system complexity, including longer tubing and mixing delays, which should be addressed in future iterations.

Figure 6C presents the results of the stock solution tests. Notably, CGM readings under constant glucose concentrations exhibited slight drift over time, rather than remaining stable (see 4.2). While internal calibration routines or environmental factors may contribute to the observed drift, one possible explanation is minor evaporation through the sensor's aperture. However, this interpretation remains speculative in the absence of direct empirical validation.

Overall, the binary system offers a reliable framework for assessing key sensor processing behaviors, while the dynamic system demonstrates the potential for algorithm-driven fluid control. The observed deviations emphasize the need to consider sensing delays and environmental influences, particularly when interpreting CGM data in non-clinical settings.

6 Conclusion

Two main CGM test rig designs, along with iterations of their parts, have been proposed in this study. The optimal supporting design choices have been concluded, including the self-constructed mixer, the open-channel interface, and a compatible tubing system. Using these choices, both systems very successfully fulfil their purposes within CGM research in an accessible, flexible, and reliable way: the binary design serves as an effective supplement for CGM accuracy stock solution tests, and the dynamic design shows promise for flexible simulation of a large range of concentrations. Both designs could help reduce both capital and labour costs associated with early-stage biosensor development. Furthermore, the rig in its current state already allows for fluid testing beyond just glucose solutions, aiding research in many more key areas.

Future work should address several key limitations and areas for improvement. Specifically, the mixing and mapping tests require further expansion, as important parameters—such as flow rate and tubing diameter—were not systematically investigated. A more rigorous experimental design, incorporating controlled environmental conditions and increased repetition, is recommended to enhance statistical reliability and strengthen the validity of the conclusions. This project has been partnered with Imperial College London's IN-CYPHER program, as our rig can be further improved to heavily aid with CGM cybersecurity research, along with accuracy. These improvements include insulin-release-associated responses, enabling its application in testing hybrid closed-loop (HCL) systems, where insulin pumps automatically release insulin based on CGM readings. Such a platform would allow testing scenarios such as the exploitation of cybersecurity vulnerabilities of CGMs or HCLs that could induce dangerous patient outcomes.

7 Acknowledgements

The team would like to sincerely thank our supervisors, Dr. Anil Bharath and Dr. Anna Bird, for their invaluable support and expertise throughout this project. We are also grateful to Dr. Pascal Egan and Dr. Tariq Malik for their expert advice and guidance in resolving electrical challenges encountered during development. Additionally, we extend our gratitude to Dr. Martyn Boutelle and Dr. Sally Gowers for granting us access to their laboratory and materials, which were instrumental in our work.

We would also like to express our appreciation to Dr. John Waldock for his assistance in manufacturing custom components, which played a crucial role in addressing issues with certain 3D prints. Finally, we extend our heartfelt thanks to all the laboratory technicians who provided support and guidance whenever we encountered difficulties.

8 Appendix

The following appendix includes project reflections, calculations of figures used in the report above, and diagrams of circuits used in the system. References can be found following the appendix.

Appendix A: Deviations from Project Pitch

Although the key ideas and processes of this project stayed largely aligned with those outlined in the project pitch, some changes had to be made due to unforeseen laboratory circumstances.

The most significant difference lies in our fluid delivery strategy. The pitch proposed two systems using syringe pumps, but the Harvard Apparatus 2000 Syringe Pumps lacked microcontroller compatibility, disqualifying them from dynamic control. As a result, open-source peristaltic pumps were adopted for the dynamic setup. This change aligned better with the goals of accessibility and controllability, albeit slightly delaying system validation. The PySerial control algorithm for the syringe pumps—developed prior to this decision—remains available as an extension of CIDARLAB's open-source repository [33].

The CGM interface design also required iteration. The T-junction introduced excessive leakage (see Section 5.4), prompting a redesign. The open-channel approach resolved this quickly and enabled effective testing conditions.

Appendix B: Project Management Lessons

Despite the team entering the project with extensive group work and large-scale project experience, many key project management lessons were learned during the completion of the project:

The largest lesson is prioritizing consistent communication on all fronts: both between the supervisor and members, and the members between themselves. There were multiple periods of time throughout the project when members of the team underwent busy periods in other areas, leading to justified communication blackouts on their side. However, these blackouts concerning one or two members often became a team-wide blackout due to perceived lack of engagement, halting progress entirely and often reverting progress due to misaligned plans and ideas left uncorrected. These busy periods in the second half of the project timeline still occurred, however by then the team had learned how to ensure that progress was still made. The most effective solution used in this project was a "Minutes" document, or detailed notes of each meeting, which was distributed consistently, ensuring those who could not attend can remain up to date and with the correct information.

Another large lesson learned is to increase documentation and organization during both the research and laboratory process. Although a shared Teams folder was created for both the members and the supervisors, many research sources, figures, models, project documents, and data sheets were communicated via alternative methods, such as a WhatsApp chat, email, or the Teams chat function, rather than uploading directly to the folder itself. Unfortunately, this resulted in lots of this information being hard to find or lost altogether, causing a large waste of time in either finding or redoing the research or 3D modelling. This issue was caught quickly during the CAD modelling stage of the project, luckily minimizing the possibility of having to redo experiments which could be costly or impossible.

Thirdly, defining a realistic scope for the project is crucial for ensuring any substantial progress. During the aims brainstorming period, shown by the project mind map found here, the aims extended far beyond the final scope of the project, requiring completing the dynamic rig in about 1/3 of the time, a very unrealistic timescale. The primary consequence of this is that during the preliminary stages of the project, the research was spread equally amongst all stages of the project, meaning that only 1-2 members of the team focused on designing the rig at the start, with the others focusing on the aims that were planned afterwards. When the specific processes and intricacies of building the rig appeared, it was clear that much time and effort was wasted on unrealistic goals, reducing the team's capabilities and progress far beyond what was originally planned.

Appendix C: Reynolds Number Range for Glucose Flow in PBS (10 mmol/L)

We calculate the Reynolds number for glucose (10 mmol/L) diluted in PBS, flowing through tubing of inner diameter $D = 1.6\,\text{mm} = 0.0016\,\text{m}$, with flow rate Q ranging from 0 to $1\,\text{mL}\,\text{min}^{-1}$.

Assumptions

- Density: $\rho = 1.022\,\text{g}\,\text{mL}^{-1} = 1022\,\text{kg}\,\text{m}^{-3}$
- Dynamic viscosity: $\mu = 0.001\,\text{Pa}\,\text{s}$
- Maximum flow rate: $Q = 1\,\text{mL}\,\text{min}^{-1} = 1.667 \times 10^{-8}\,\text{m}^3\,\text{s}^{-1}$

Reynolds Number Derivation

$$\text{Re} = \frac{\rho v D}{\mu}, \quad \text{with } v = \frac{Q}{A} = \frac{4Q}{\pi D^2}$$

$$\Rightarrow \text{Re} = \frac{\rho D}{\mu} \cdot \frac{4Q}{\pi D^2} = \frac{4\rho Q}{\pi D \mu}$$

Substitute Values

$$\text{Re} = \frac{4 \cdot 1022 \cdot Q}{\pi \cdot 0.0016 \cdot 0.001} = \frac{4.088 \times 10^6 \cdot Q}{\pi \cdot 0.0016}$$

At Maximum Flow Rate

$$Q = 1.667 \times 10^{-8}\,\text{m}^3\,\text{s}^{-1} \Rightarrow \text{Re}_{\max} = \frac{4 \cdot 1022 \cdot 1.667 \times 10^{-8}}{\pi \cdot 0.0016 \cdot 0.001} = \frac{6.813 \times 10^{-5}}{5.0265 \times 10^{-6}} \approx 13.6$$

At Zero Flow

$$Q = 0 \Rightarrow \text{Re} = 0$$

Final Reynolds Number Range

$$\boxed{0 \leq \text{Re} \leq 13.6}$$

Appendix D: Reynolds and Dean Numbers

The Reynolds number is calculated as:

$$Re = \frac{\rho v D}{\mu} = \frac{v D}{\nu}$$

where ρ is fluid density (kg/m^3), v is velocity (m/s), D is tubing diameter (m), μ is dynamic viscosity (Pa·s), and ν is kinematic viscosity (m^2/s).

Dean number is defined as:

$$De = Re \cdot \sqrt{\frac{R}{R_c}}$$

where R is tube radius and R_c is bend radius.

Appendix E: Peristaltic Pump Development Support

The bill of materials and parts list can be found in the file labelled "readme.md" in the folder labelled "pump 1_1," found under:
`https://github.com/Synthetic-Automated-Systems/open_micro_pump/tree/main/pump1_1`

Any changes can be found in the team's repository in "Peristaltic Pump Part Customizations," at:
https://github.com/sunon4/CGM-test-rig-ICL-Bioeng-/tree/3D-Models/Peristaltic%20Pump%20Part%20Customizations/peristaltic

The assembly instructions can be found in the file labelled "Appendix A assembly instructions.pdf" in the open-source GitHub link, found under:
https://github.com/Synthetic-Automated-Systems/open_micro_pump/blob/main/Appendix%20A%20assembly%20instructions.pdf

The Control Algorithm Code can be found in the "pumpcontrol" branch in the team's GitHub repository:
https://github.com/sunon4/CGM-test-rig-ICL-Bioeng-/tree/arduino/3dprintingpumpcontrol

The Padova Model example case as well as information about it can be found here:
https://github.com/jxx123/simglucose/blob/master/examples/results/2017-12-31_17-46-32/adult%23006.csv

Sample Calculation for Volumetric Flow Rate:

$$Q = \frac{\text{Mass}}{\text{Density} \times \text{Minutes} \times \text{Number of Pumps}}$$

$$Q = \frac{179.2}{1.0218 \times 10 \times 2} = 8.76 \text{ mL/min}$$

This yields the data point **(150 RPM, 8.76 mL/min)**.

Appendix F – Material List for Binary Design

Part Name	**Manufacturer / Retailer**	**Purchasing Website**	**Qty.**
Sourcing Map Mini Solenoid Valve	Sourcing map / Amazon	https://www.amazon.co.uk/sourcing-map-Miniature-Solenoid-Position/dp/B07VR88F24/	2
Double Lumen Extension Y-Set Bionect	Vygon / UK MEDI	https://ukmedi.co.uk/products/double-lumen-extension-y-set-bionect-vygon-841-ukmedi-co-uk	1
Syringe Adapter, Clear Male Luer Lock 1/16"	AIEX / Amazon	https://www.amazon.co.uk/Syringe-Adapter-Clear-Male-Luer-Connector-Kit-Coupler/dp/B0BMDVDT1T/	9
PVC Transparent Hose Tubing 1.5mm ID 2mm OD, 2m	Sourcing map / Amazon	https://www.amazon.co.uk/sourcing-map-Transparent-Flexible-Lightweight/dp/B09DGDQ29M?th=1	1
T Connector, Individual	Vets4u	https://www.vets4u.uk/buster-classic-transparent-collar-75cm-box-of-10-pieces	1

Table 3: Material list for the binary design

Appendix G – Material List for Dynamic Design

Part Name	Manufacturer / Retailer	Purchasing Website	Qty.
Double Lumen Extension Y-Set Bionect	Vygon / UK MEDI	https://ukmedi.co.uk/products/double-lumen-extension-y-set-\protect\@normalcr\relaxbionect-vygon-841-ukmedi-co-uk	1
Syringe Adapter, Clear Male Luer Lock 1/16”	AIEX / Amazon	https://www.amazon.co.uk/Syringe-Adapter-Clear-Male-Luer-\protect\@normalcr\relaxConnector-Kit-Coupler/dp/B08MDVDT1T/	3
PVC Transparent Hose Tubing 1.5mm ID 2mm OD, 2m	Sourcing map / Amazon	https://www.amazon.co.uk/sourcing-map-Transparent-Flexible\protect\@normalcr\relax-Lightweight/dp/B09DGDQ29M?th=1	1
T Connector, Individual	Vets4u	https://www.vets4u.uk/buster-classic-transparent-\protect\@normalcr\relaxcollar-75cm-box-of-10-pieces	1
iMetrix Nema 17 Stepper Motor	iMetrix / Amazon	https://www.amazon.co.uk/iMetrix-stepper-1-5A-3-8V-\protect\@normalcr\relaxCreality-extruder/dp/B097JXK9VV/	1
Accu - M3 x 16mm Full Thread Screws	Accu / Amazon	https://www.amazon.co.uk/dp/B0CJFMF9QX/	1
TERF M3 X 40mm Hex Socket Cap Head	TERF / Amazon	https://www.amazon.co.uk/Socket-Machine-Screws-Stainless-Hexagonal/dp/B08SW8FPB8/	1
METALLIXITY Hex Nuts (M3×0.5mm)	METALLIXITY / Amazon	https://www.amazon.co.uk/METALLIXITY-M3x0-5mm-Stainless-\protect\@normalcr\relaxHexagon-Hardware/dp/B0CW9C9PJR/	1
Kozelo 15pcs 626-ZZ Deep Groove Bearings	Kozelo / Amazon	https://www.amazon.co.uk/Kozelo-15pcs-626-ZZ-Groove-\protect\@normalcr\relaxBearings/dp/B0C2D92ZCL/	1
Linear Motion Rod Shaft Guide 6mm x 100mm	Sourcing map / Amazon	https://www.amazon.co.uk/sourcing-map-Hardened-Printer-\protect\@normalcr\relaxMachine/dp/B0D15X9KS/	1
Silicone Tubing, 0.5mm ID x 1.5mm OD, 16.4ft	Sourcing map / Amazon	https://www.amazon.co.uk/sourcing-map-Silicone-Tubing-0-\protect\@normalcr\relax5mm/dp/B0DTYX378M/	1
HiPicco R166ZZ Ball Bearings, 3/16”x3/8”x1/8”	HiPicco / Amazon	https://www.amazon.co.uk/gp/product/B0CH35V832/	1
Arduino Uno Rev3	RS	https://uk.rs-online.com/web/p/arduino/7154081	1
DollaTek 5Pcs A4988 Stepper Driver Modules	DollaTek / Amazon	https://amzn.eu/d/bNZOaw6	1

Table 4: Material list for components used in the dynamic fluidic control design.

Appendix H: Custom Input Glucose Profile for Dynamic System Tests

The custom glucose profile tests edge cases, as well as the ideal pump spacing, however it lacks the delay calculation which proved to be problematic.

$$[\text{Solution}]\ (\text{mmol/L}) = \begin{cases} 20 & \text{for } 0 < t < 30 \text{ min} \\ 10 & \text{for } 30 < t < 60 \text{ min} \\ 15 & \text{for } 60 < t < 120 \text{ min} \end{cases}$$

Appendix I: GrabCAD Mixer Link

PVC in-line mixer (McMaster Part #35385K22) by David Parrott:
`https://grabcad.com/library/pvc-in-line-mixer-mcmaster-part-35385k22-1`

Appendix J: Red Dye Ingredients

The red dye used was Tropical Sun Red Colouring. Ingredients: Water, Carmoisine (E122), Acetic Acid [34].

Appendix K: Density Calculation

Step 1: Mass of PBS
For 1 L (1000 mL) of PBS:

$$\text{Mass of PBS} = 1000\,\text{mL} \times 1.02\,\text{g/mL} = 1020\,\text{g}$$

Step 2: Mass of Glucose

- Molar mass of glucose ($C_6H_{12}O_6$):

$$6(12.01) + 12(1.008) + 6(16.00) = 180.16\,\text{g/mol}$$

- Mass of glucose in a 10 mmol/L solution:

$$0.01\,\text{mol/L} \times 180.16\,\text{g/mol} = 1.8016\,\text{g/L}$$

Step 3: Total Mass of Solution

$$\text{Total mass} = \text{Mass of PBS} + \text{Mass of glucose} = 1020\,\text{g} + 1.8016\,\text{g} = 1021.8016\,\text{g}$$

Step 4: Density of the Solution
Assuming the volume remains approximately 1 L (1000 mL) due to the low glucose concentration:

$$\text{Density} = \frac{\text{Total mass}}{\text{Volume}} = \frac{1021.8016\,\text{g}}{1000\,\text{mL}} = 1.0218\,\text{g/mL}$$

Appendix L: Glucose Control Algorithm Sample Calculation

To demonstrate the control logic, we calculate the system parameters at the first time point using the following user inputs:

- Composite flow rate: $Q_{\text{total}} = 10.0$ mL/min
- Channel internal diameter: $D = 1.5$ mm
- Pre-intersection channel length: $L = 10.0$ mm
- High glucose concentration: $C_1 = 15$ mmol/L
- Low concentration (PBS): $C_2 = 0$ mmol/L
- First recorded concentration: 158.0176 mg/dL

1. Calculate Pump Flow Rates

$$C_{\text{target}} = \frac{158.0176}{18.01559} = 8.7712 \text{ mmol/L}$$

$$Q_{\text{glucose}} = Q_{\text{total}} \cdot \frac{C_{\text{target}} - C_2}{C_1 - C_2} = 10.0 \cdot \frac{8.7712 - 0}{15 - 0} = 5.8475 \text{ mL/min}$$

$$Q_{\text{PBS}} = Q_{\text{total}} - Q_{\text{glucose}} = 10.0 - 5.8475 = 4.1525 \text{ mL/min}$$

2. Calculate Flow Velocities and Delays

Convert flow rates to m^3/s:

$$Q_1 = \frac{5.8475}{60 \times 10^6} = 9.7458 \times 10^{-9} \text{ m}^3/\text{s} \qquad Q_2 = \frac{4.1525}{60 \times 10^6} = 6.9208 \times 10^{-9} \text{ m}^3/\text{s}$$

Cross-sectional area:

$$r = \frac{1.5}{2 \cdot 1000} = 0.00075 \text{ m}, \quad A = \pi r^2 = \pi \cdot (0.00075)^2 = 1.7671 \times 10^{-6} \text{ m}^2$$

Velocities:

$$v_1 = \frac{Q_1}{A} = \frac{9.7458 \times 10^{-9}}{1.7671 \times 10^{-6}} = 0.005515 \text{ m/s} \qquad v_2 = \frac{Q_2}{A} = 0.003917 \text{ m/s}$$

$$t_1 = \frac{0.010}{0.005515} = 1.813 \text{ s}, \quad t_2 = \frac{0.010}{0.003917} = 2.552 \text{ s}$$

$$\Delta t = |t_1 - t_2| = 0.739 \text{ s} = 739 \text{ ms}$$

Since PBS takes longer, the glucose pump must be delayed:

$$\text{Delay}_{\text{glucose}} = 739 \text{ ms}, \quad \text{Delay}_{\text{PBS}} = 0 \text{ ms}$$

3. Convert Flow Rate to RPM

$$\text{RPM}_{\text{Pump 1}} = \left\lfloor \frac{Q_{\text{glucose}} + 0.2537}{0.1185} \right\rfloor = \left\lfloor \frac{6.1012}{0.1185} \right\rfloor = 51$$

$$\text{RPM}_{\text{Pump 2}} = \left\lfloor \frac{4.4062}{0.1185} \right\rfloor = 37$$

4. Final Output Line

```
Second 0 | Target Conc: 8.77116 M | G Flow: 5.848 mL/min | PBS Flow: 4.152 mL/min
| Delay G: 739 ms | Delay P: 0 ms | Pump 1 RPM: 51 | Pump 2 RPM: 37
```

Appendix M: FreeStyle Libre2's Filament

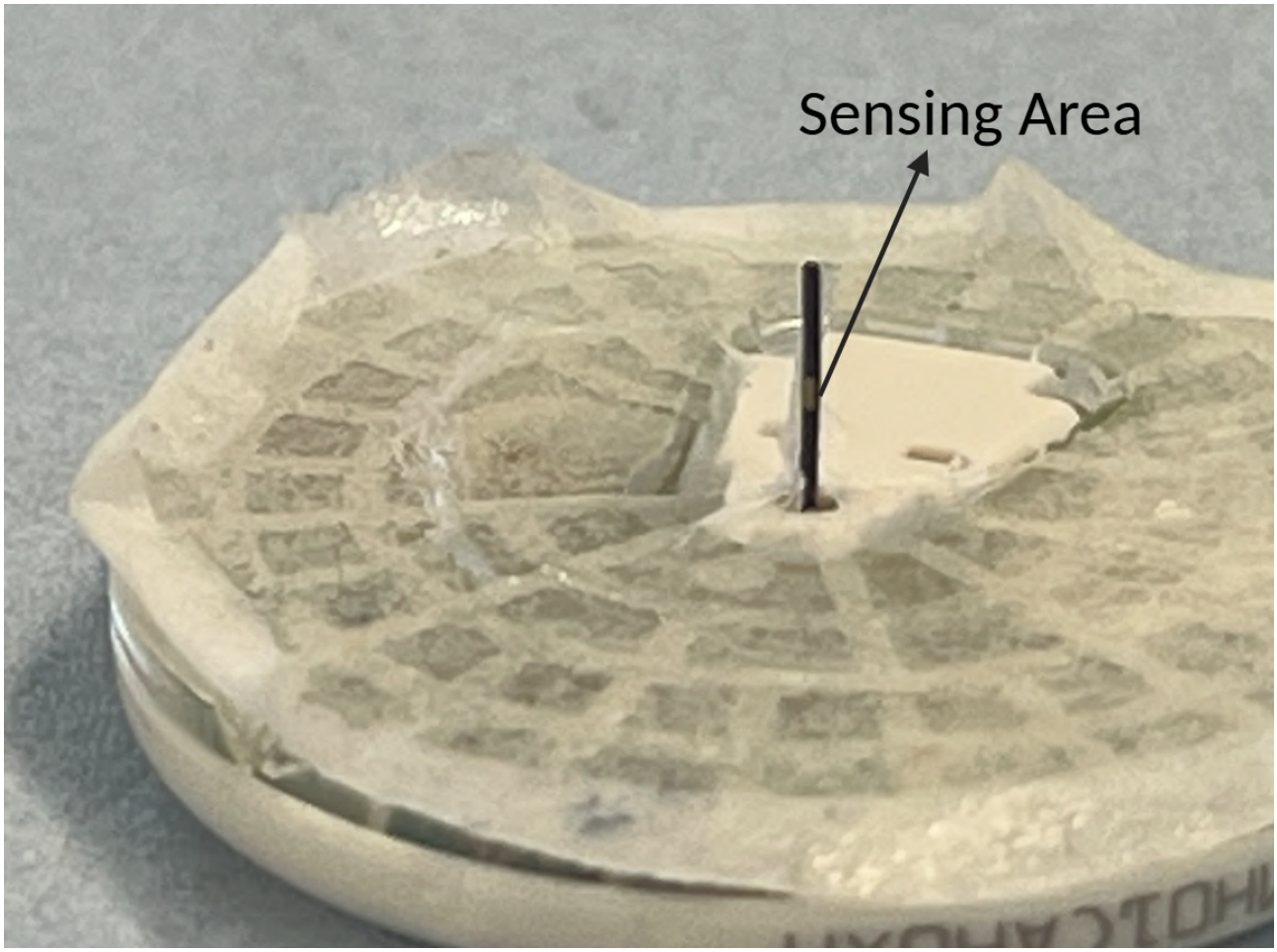

Figure 10: FreeStyle Libre2's Filament: The filament has a diameter of 0.4 mm and a length of 5 mm [35]. The silver-colored region at the tip serves as the sensing area of the continuous glucose monitor (CGM), which must be fully immersed in the target fluid for accurate measurement.

Appendix N: Original Peristaltic Pump Design Featuring Gear Train

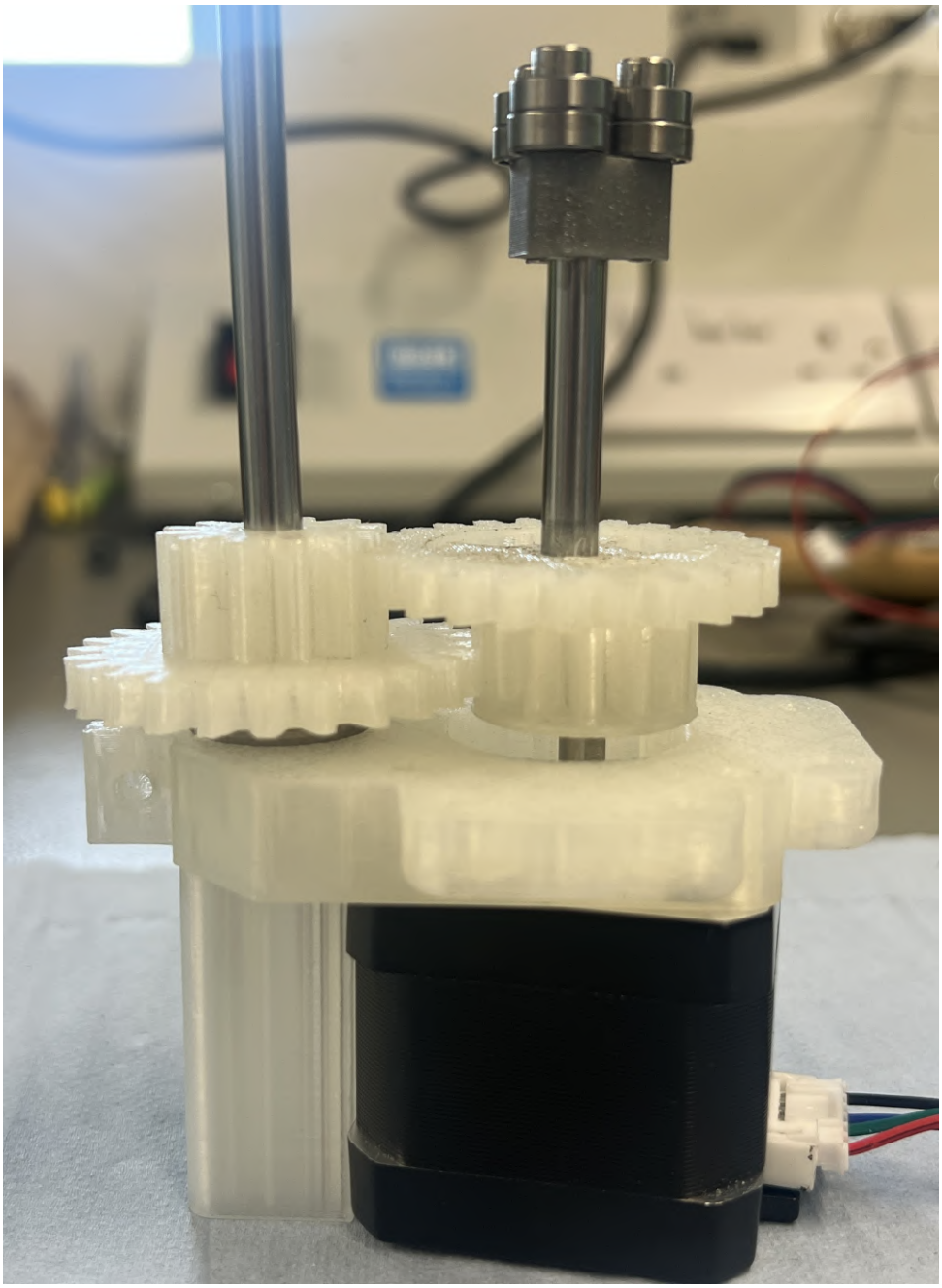

Figure 11: Original Peristaltic Pump Design Featuring Gear Train

To reduce mechanical vibrations and structural instability observed during operation, several modifications were implemented, primarily targeting the torque transmission system between the stepper motor and the rotor shaft. The original design utilized a gear train comprising a motor-mounted gear, intermediary side gears, and a rotor-mounted gear, all connected via pin joints. While effective for basic torque transfer, these joints inherently allowed slight mechanical play, which introduced deviations from the intended rotational axis. This, in turn, led to oscillations of the pump assembly and misalignment of the fluidic tubing, significantly impairing overall pumping performance.

To address these limitations, the gear train was replaced with a direct set screw coupling between the motor and rotor shafts(Figure 7A). This revised configuration eliminated intermediary gears and significantly reduced mechanical backlash. Moreover, the set screw coupling was more effective at accommodating minor misalign-

ments while preserving torque fidelity, thereby improving mechanical stability and enhancing the consistency of fluid delivery.

Appendix O: Circuits

Valves-Controlled Circuit

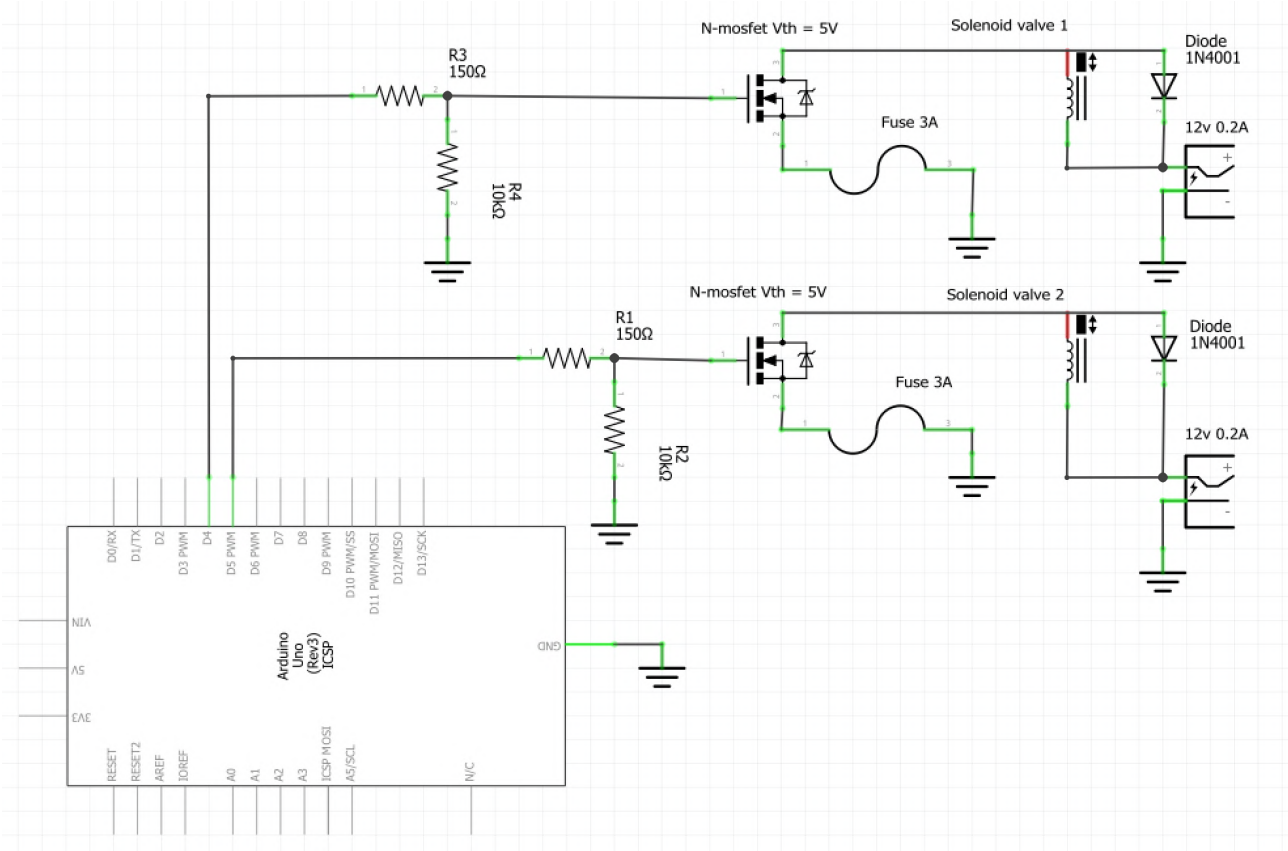

Figure 12: Circuit Schematic for Dual-Valve Control System

A 12 V DC power supply is connected to one terminal of the solenoidal valve, with the other terminal connected to ground. Between the solenoidal valve and ground, two protective components are placed in series: a 3 A fuse and an N-channel MOSFET switch.

The fuse provides overcurrent protection, preventing damage to circuit components by breaking the connection if the current exceeds 3 A. The MOSFET functions as a low-side switch and is controlled by a digital output from an Arduino. The gate of the MOSFET is driven by a 5 V signal, which is equal to the device's threshold voltage $V_{\text{gs(th)}} = 5\,\text{V}$. A series resistor is included to protect the gate, but its resistance is sufficiently low that it does not significantly reduce the gate voltage.

When a HIGH signal (5 V) is applied to the gate, the MOSFET turns on, completing the circuit and energizing the solenoidal valve. Conversely, when a LOW signal (0 V) is applied, the MOSFET turns off, leaving the circuit open and deactivating the valve.

In addition, a diode is connected in reverse-bias across the peristaltic pump. This flyback diode protects the circuit from voltage spikes generated by the inductive nature of the motor. When the pump is switched off, the back electromotive force (EMF) caused by the collapsing magnetic field is safely dissipated through the diode, preventing potential damage to sensitive control components.

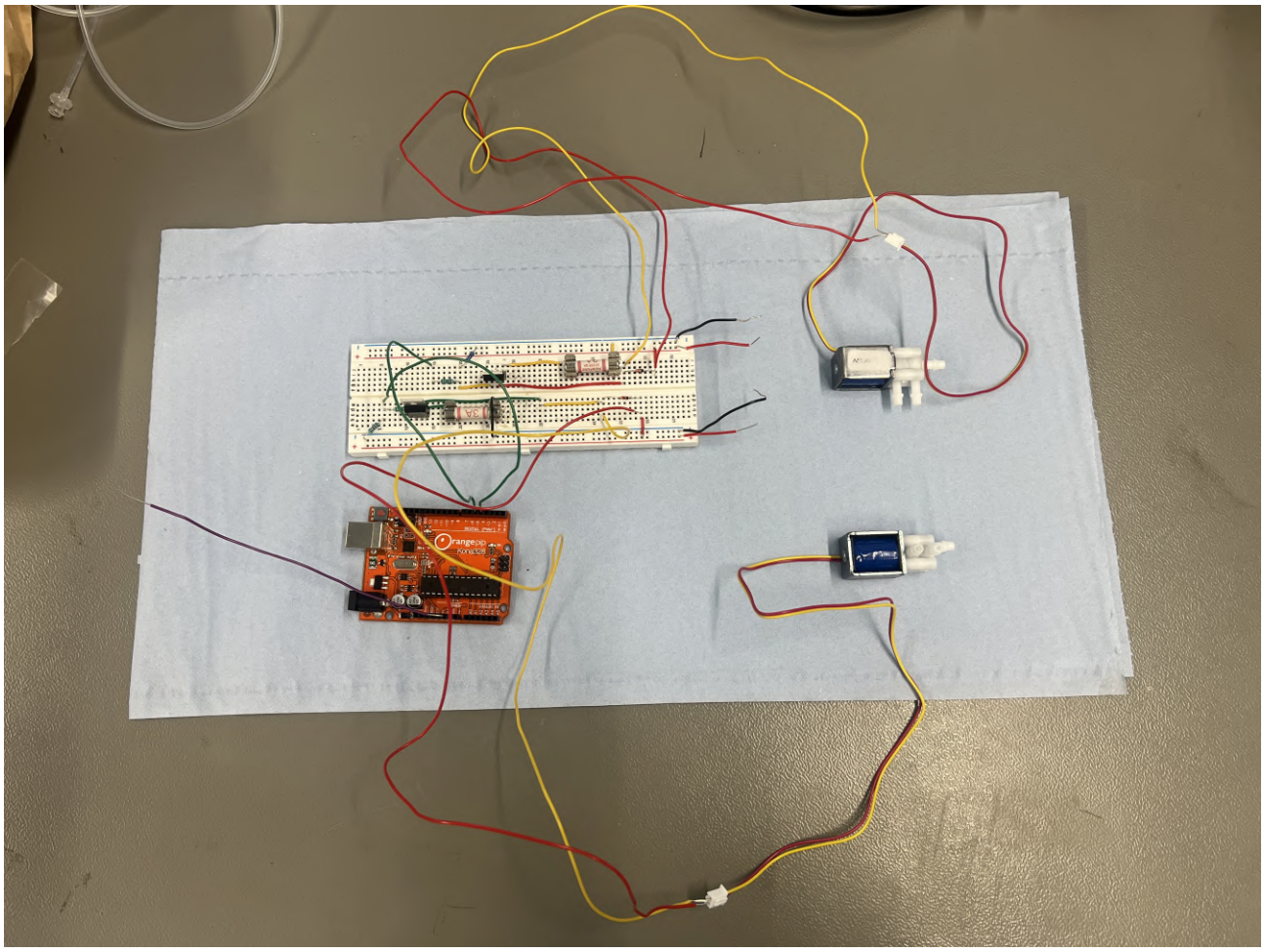

Figure 13: Physical Two-Valve Control Circuit

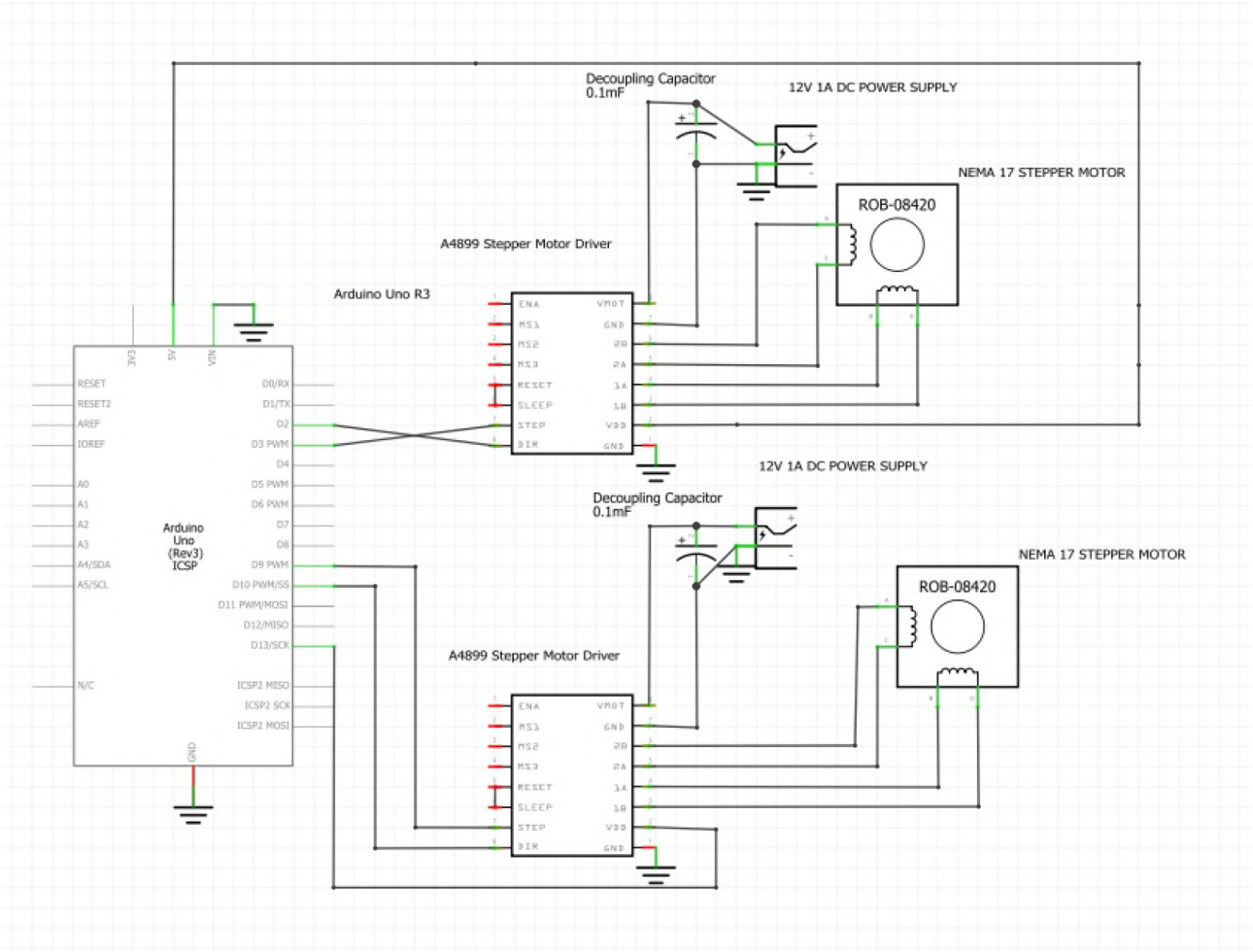

Figure 14: Circuit Schematic for Dual-Pump Control System

The NEMA 17 stepper motor is controlled via an A4988 stepper motor driver, interfaced with an Arduino Uno R3. The Arduino provides two digital control signals:

- **STEP**: Each rising edge on this pin advances the motor by one full step.
- **DIR**: Determines the direction of rotation; a HIGH signal sets one direction, while a LOW signal sets the other.

A 12 V, 2 A external DC power supply is used to power the motor via the A4988's `VMOT` input. A 100 μF capacitor is placed across the power supply terminals to buffer voltage spikes and absorb electrical noise. The driver's logic circuitry is powered by the Arduino's 5 V output connected to the `VDD` pin.

The motor coils are connected to the A4988's `OUT1A/OUT1B` and `OUT2A/OUT2B` terminals. Current limiting is configured using the onboard potentiometer to prevent the motor from exceeding its rated current. Although the A4988 supports microstepping via the `MS1--3` pins, this setup operates in full-step mode for simplicity.

The Arduino generates a pulse train on the `STEP` pin to control motor speed, where the RPM is proportional to the pulse frequency. The total number of pulses determines the rotation angle, and the `DIR` pin is set before stepping begins.

Pumps-Controlled Circuit

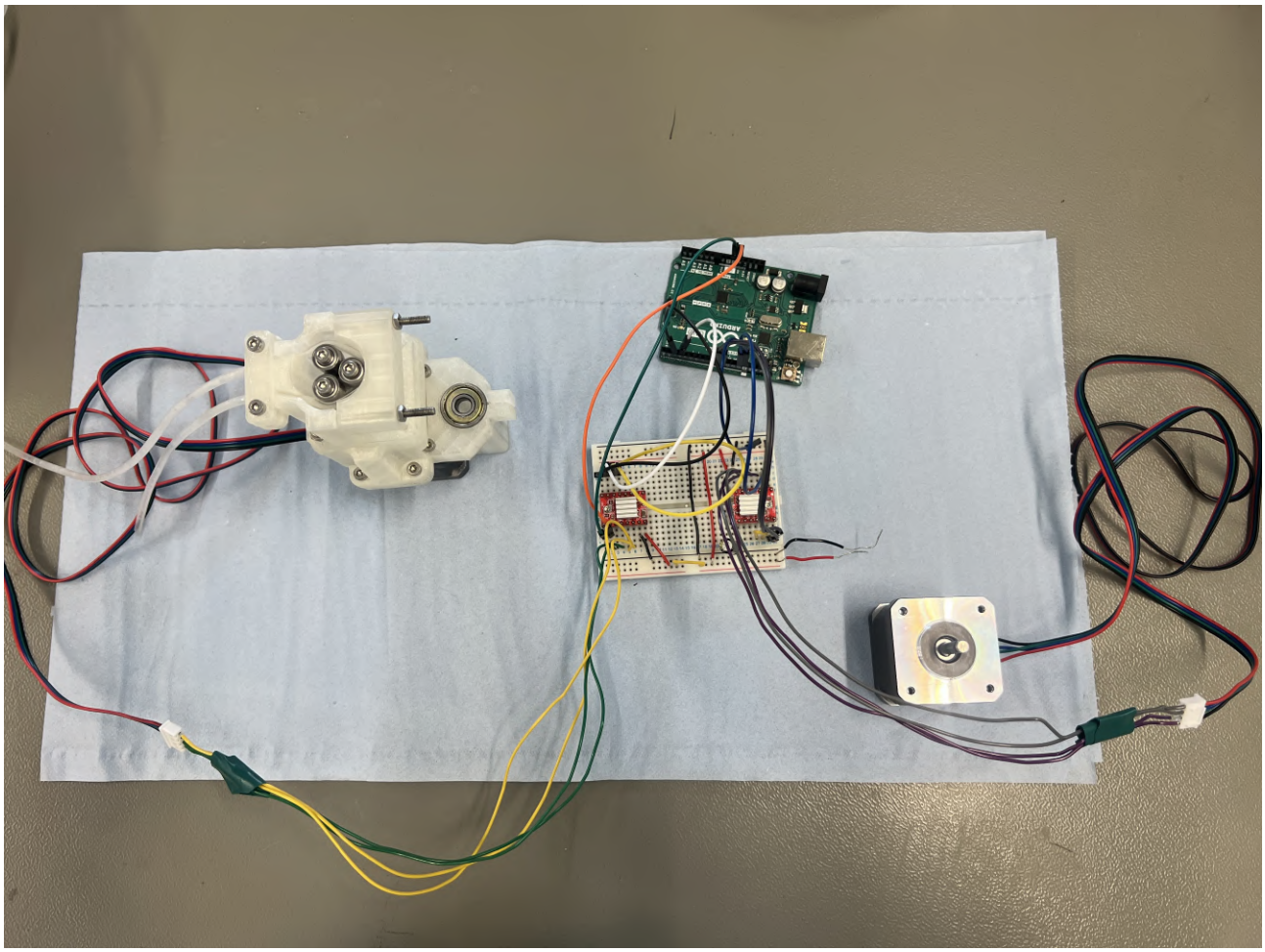

Figure 15: Physical Two-Pump Control Circuit

Appendix P: Control Algorithm Edge Case Behaviour Calculation

To demonstrate the experimental conditions where the algorithm outputs a necessary but problematic delay value for our system, we calculate the system parameters at the first time point using the following user inputs:

- Composite flow rate: $Q_{\text{total}} = 2.0$ mL/min
- Channel internal diameter: $D = 1.5$ mm
- Pre-intersection channel length: $L = 100.0$ mm
- High glucose concentration: $C_1 = 20$ mmol/L
- Low concentration (PBS): $C_2 = 8.5$ mmol/L
- First recorded concentration: 158.0176 mg/dL

1. Calculate Pump Flow Rates

$$C_{\text{target}} = \frac{158.0176}{18.01559} = 8.7712 \text{ mmol/L}$$

$$Q_{\text{glucose}} = Q_{\text{total}} \cdot \frac{C_{\text{target}} - C_2}{C_1 - C_2} = 2.0 \cdot \frac{8.7712 - 8.5}{20 - 8.5} = 0.047 \text{ mL/min}$$
$$Q_{\text{PBS}} = Q_{\text{total}} - Q_{\text{glucose}} = 2.0 - 0.047 = 1.953 \text{ mL/min}$$

2. Calculate Flow Velocities and Delays

Convert flow rates to m^3/s:

$$Q_1 = \frac{0.047}{60 \times 10^6} = 7.833 \times 10^{-10} \text{ m}^3/\text{s} \qquad Q_2 = \frac{1.953}{60 \times 10^6} = 3.255 \times 10^{-8} \text{ m}^3/\text{s}$$

Cross-sectional area:

$$r = \frac{1.5}{2 \cdot 1000} = 0.00075 \text{ m}, \quad A = \pi r^2 = \pi \cdot (0.00075)^2 = 1.7671 \times 10^{-6} \text{ m}^2$$

Velocities:

$$v_1 = \frac{Q_1}{A} = \frac{7.833 \times 10^{-10}}{1.7671 \times 10^{-6}} = 0.000443 \text{ m/s} \qquad v_2 = \frac{Q_2}{A} = 0.01843 \text{ m/s}$$
$$t_1 = \frac{0.100}{0.000443} = 225.7 \text{ s}, \quad t_2 = \frac{0.100}{0.01843} = 5.43 \text{ s}$$
$$\Delta t = |t_1 - t_2| = 220.3 \text{ s} = 220300 \text{ ms}$$

Since glucose takes longer, the PBS pump must be delayed:

$$\text{Delay}_{\text{glucose}} = 0 \text{ ms}, \quad \text{Delay}_{\text{PBS}} = 220300 \text{ ms} = \frac{220300}{1000 \times 60} \approx \mathbf{3.67} \text{ min}$$

9 Reference

References

[1] Ming Yeh Lee, Seav SM, Loice Ongwela, Lee JJ, Aubyrn R, Cao FY, et al. Empowering hospitalized patients with diabetes: Implementation of a hospital-wide cgm policy with ehr-integrated validation for dosing insulin. *Diabetes Care*, 2024. https://doi.org/10.2337/dc24-0626.

[2] Battelino T, Alexander CM, Amiel SA, Arreaza-Rubin G, Beck RW, Bergenstal RM, et al. Continuous glucose monitoring and metrics for clinical trials: an international consensus statement. *The Lancet Diabetes Endocrinology*, 11(1):42–57, 2023. https://doi.org/10.1016/s2213-8587(22)00319-9.

[3] Tong X, Jiang T, Yang J, Song Y, Ao Q, Tang J, et al. Continuous glucose monitoring (cgm) system based on protein hydrogel anti-biofouling coating for long-term accurate and point-of-care glucose monitoring. *Biosensors and Bioelectronics*, 277:117307–117307, 2025. https://doi.org/10.1016/j.bios.2025.117307.

[4] Pfützner A, Hendrick Jensch, Cardinal C, Geetham Srikanthamoorthy, Riehn E, and Thomé N. Laboratory protocol and pilot results for dynamic interference testing of continuous glucose monitoring sensors. *Journal of Diabetes Science and Technology*, pages 193229682210955–193229682210955, 2022. https://doi.org/10.1177/19322968221095573.

[5] Saha T, Rafael Del Caño, Kuldeep Mahato, De E, Chen C, Ding S, et al. Wearable electrochemical glucose sensors in diabetes management: A comprehensive review. *Chemical Reviews*, 123(12):7854–7889, 2023. https://doi.org/10.1021/acs.chemrev.3c00078.

[6] Schiavon M, Dalla Man C, Dube S, Slama M, Kudva YC, Peyser T, et al. Modeling plasma-to-interstitium glucose kinetics from multitracer plasma and microdialysis data. *Diabetes Technology Therapeutics*, 17(11):825–831, 2015. https://doi.org/10.1089/dia.2015.0119.

[7] Harvard Apparatus. Syringe pump series user's manual publication 5400-008-rev-f. 2025. [Accessed 12th April 2025].

[8] Facchinetti A, Sparacino G, and Cobelli C. Reconstruction of glucose in plasma from interstitial fluid continuous glucose monitoring data: Role of sensor calibration. *Journal of Diabetes Science and Technology*, 1(5):617–623, 2007. https://doi.org/10.1177/193229680700100504.

[9] Ribet F, Dobielewski M, Böttcher M, Beck O, Stemme G, and Roxhed N. Minimally invasive and volume-metered extraction of interstitial fluid: bloodless point-of-care sampling for bioanalyte detection. 2020. [Accessed 12th April 2025].

[10] Bösch PC, Fougner AL, Ellingsen R, Dag Roar Hjelme, and Øyvind Stavdahl. Test-rig for automated testing of continuous glucose sensor prototypes. *ResearchGate*, 2018. https://doi.org/10.13140/RG.2.2.34841.72809.

[11] M. R. Behrens, H. C. Fuller, E. R. Swist, J. Wu, M. M. Islam, Z. Long, et al. Open-source, 3d-printed peristaltic pumps for small volume point-of-care liquid handling. *Scientific Reports*, 10(1):1543, 2020.

[12] Rodrigo Hernández Vera, Genové E, Alvarez L, Borrós S, Kamm R, Lauffenburger D, et al. Interstitial fluid flow intensity modulates endothelial sprouting in restricted src-activated cell clusters during capillary morphogenesis. *Tissue Engineering Part A*, 15(1):175–185, 2009. https://doi.org/10.1089/ten.tea.2007.0314.

[13] Harvard Apparatus. *PHD 22/2000 Syringe Pump Series User's Manual*, n.d. Accessed 2025-04-14.

[14] Hansel BC. Managing luer connections. *Anesthesia Patient Safety Foundation*, 2021. https://www.apsf.org/article/managing-luer-connections/.

[15] IQS Directory. Static mixers: What is it? how does it work? uses. *iqsdirectory.com*. https://www.iqsdirectory.com/articles/mixer/static-mixers.html.

[16] J. Klymak. Physics 426 fluid mechanics. laminar flow. https://jklymak.github.io/Phy426/lab_demos20/Laminar_Dean_Thomas/, 2025. Accessed 2025-04-14.

[17] Prasun Dutta, Sumit Kumar Saha, Nityananda Nandi, and Nairit Pal. Numerical study on flow separation in 90° pipe bend under high reynolds number by k- modelling. *Engineering Science and Technology, an International Journal*, 19(2):904–910, 2016.

[18] M. G. Sánchez-Salazar, R. Garza-Garza, R. Crespo-López Oliver, V. S. Jerezano-Flores, S. Gallegos-Martínez, S. Ramos-Meizoso, et al. Continuous inline monitoring of glucose in an organ-on-chip using freestyle™ libre glucometers. *Frontiers in Lab on a Chip Technologies*, 3, 2024.

[19] Abbott Diabetes Care. *FreeStyle Libre 2 — A New ICGM Device*, 2020. Accessed 2025-04-14.

[20] Eda Cengiz and William V. Tamborlane. A tale of two compartments: Interstitial versus blood glucose monitoring. *Diabetes Technology & Therapeutics*, 11(S1):S11–S16, 2009.

[21] Steven Farmer, Dietmar Kennepohl, and William Reusch. 25.5: Cyclic structures of monosaccharides - anomers, n.d. Accessed 2025-04-14.

[22] B. J. van Enter and E. von Hauff. Challenges and perspectives in continuous glucose monitoring. *Chemical Communications*, 54(4):532–545, 2018.

[23] Song H, Tice JD, and Ismagilov RF. A microfluidic system for controlling reaction networks in time. *Angewandte Chemie*, 115(7):792–796, 2003. https://doi.org/10.1002/ange.200390172.

[24] The GrabCAD Community. Free cad designs, files 3d models — the grabcad community library. Grab-

cad.com, 2025. [Accessed 15th April 2025].

[25] Jenway. *Spectrophotometer 6305 Instruction Manual*, n.d. Available from: https://pim-resources.coleparmer.com/instruction-manual/99968-68-jenway-6305-rev-j-instruction-manual.pdf.

[26] NASA. Visible light. https://science.nasa.gov/ems/09_visiblelight/, n.d. Accessed 2025-04-14.

[27] SIGMA. Product information. SIGMA. [Accessed 15th April 2025].

[28] Synthetic-Automated-Systems. Github - synthetic-automated-systems/open$_{m}icro_{p}ump$: $3dpartsfilesandcodeforcreatinglowcostperistalticpumpsformicrofluidics.GitHub$, 2025.[$Accessed12thApril2025$].

[29] Chiara Dalla Man, Francesco Micheletto, Dayu Lv, Marc Breton, Boris Kovatchev, and Claudio Cobelli. The uva/padova type 1 diabetes simulator. *Journal of Diabetes Science and Technology*, 8:26–34, 01 2014.

[30] Francis Lin, Wajeeh Saadi, Seog Woo Rhee, Shur-Jen Wang, Sukant Mittal, and Noo Li Jeon. Generation of dynamic temporal and spatial concentration gradients using microfluidic devices. *Lab on a Chip*, 4(3):164–167, 2004.

[31] Battelino T, Danne T, and Bergenstal RM. Clinical targets for continuous glucose monitoring data interpretation: Recommendations from the international consensus on time in range. *Diabetes Care*, 42(8):1593–1603, 2019. https://doi.org/10.2337/dci19-0028.

[32] Spirit Medical. Single lumen, luer-lock t-piece connector with microbore extension set, 10cm - secureconnect®. https://spiritmedical.com/products/secureconnect/secureconnect-closed-needle-free-single-lumen-luer-lock-t-connector-microbore-extension-set-10cm/, 2023. Accessed 2025-04-13.

[33] CIDARLAB. Syringe pumps github repository. https://github.com/CIDARLAB/syringe_pumps/tree/main, 2023. Accessed 2025-04-13.

[34] Tropical Sun. Red colouring (28ml). https://longdan.co.uk/products/tropical-sun-red-colouring-28ml, 2025. Accessed 2025-04-13.

[35] Abbott Kuwait. Freestyle libre faqs. https://www.freestyle.abbott/kw-en/discover-freestyle-libre/why-freestyle-libre-/what-are-the-components-of-the-freestyle-libre-system.html, 2022.